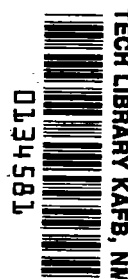


NASA Technical Paper 1166

LOAN COPY: RETURN TO
AFWL TECHNICAL LIBRARY
KIRTLAND AFB, N. M.

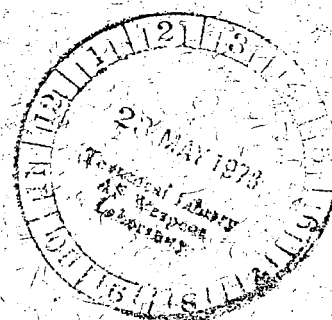


Comparison of Two Computer Programs by Predicting Turbulent Mixing of Helium in a Ducted Supersonic Airstream

Y. S. Pan, John Philip Drummond,
and Charles R. McClinton

MAY 1978

NASA





NASA Technical Paper 1166

Comparison of Two Computer Programs by Predicting Turbulent Mixing of Helium in a Ducted Supersonic Airstream

Y. S. Pan, John Philip Drummond,
and Charles R. McClinton
Langley Research Center
Hampton, Virginia



National Aeronautics
and Space Administration

**Scientific and Technical
Information Office**

1978

SUMMARY

The traditional approach for combustor development, based on cut-and-try experimentation, is very costly, and the designer of supersonic combustors has encountered difficulties in the acquisition of meaningful data. Recent advances in computational capabilities have made it possible to predict complex flow fields in combustors. Such computational approaches could supplement the traditional experimentation and help overcome some of the difficulties in supersonic combustor development.

Two parabolic flow computer programs, one based on a finite-difference method and the other on a finite-element method, are used at the NASA Langley Research Center. Both programs are capable of predicting three-dimensional turbulent reacting flow fields in supersonic combustors. A three-dimensional turbulent mixing experiment has been conducted for detailed evaluation of the two computer programs. To alleviate the difficulties associated with high-temperature measurements, a cold (nonreacting) flow experiment was performed to study the mixing of helium jets with a supersonic airstream in a rectangular duct. Surveys of the flow field were made at two stations downstream of the injectors. The flow surveys at the upstream station were used as initial data by both computer programs. The surveys at the downstream station provided an experimental comparison to assess the relative accuracies of the two programs. Computational efficiencies were also compared.

In this paper, the theoretical foundations of the two computer programs are first introduced. The three-dimensional mixing experiment and the application of two computer programs to that experiment are then described. Finally, comparisons between the two computations and between the computations and the experiment are made. In general, both computer programs predicted the experimental results and data trends reasonably well. However, the comparison indicated that the finite-difference program was more accurate in computation and more efficient in both computer storage and computing time than the present version of the finite-element program.

INTRODUCTION

Recent advances in computational techniques and computer capabilities have made it possible to predict three-dimensional turbulent reacting flow fields. Such analytical predictions are extremely valuable in the development of supersonic combustors for planned hypersonic airbreathing engines. The traditional approach for such combustor development has been based on expensive cut-and-try experimentation.

At present, two computer programs, SHIP (ref. 1) and COMOC (ref. 2), which are capable of predicting three-dimensional turbulent flow fields in supersonic combustors, are operational at the NASA Langley Research Center. SHIP is based on a finite-difference algorithm of Spalding (ref. 3) and COMOC is based on a

finite-element algorithm of Baker (ref. 4). The mathematical foundations and the relative merits of the two algorithms are well known; successful computations using these algorithms have appeared in the open literature (for example, refs. 2, 3, and 5 to 8). However, direct comparisons between these two computer programs have not been made to assess their computational capabilities, turbulence models, numerical schemes, and results. The objective of this paper is to make such direct comparisons to assess both programs as combustor design tools. To aid in accomplishing this objective, a three-dimensional mixing flow experiment has been conducted and both computer programs have been applied to predict the experimental flow field.

In the past, the two computer programs were applied separately to a mixing flow field with normal injection of hydrogen into a supersonic airstream (ref. 9). However, meaningful comparisons were not possible because of different approaches to handling the same flow problem. The finite-element program was applied downstream of the injection by modeling the normal injection with an equivalent one-dimensional virtual source (ref. 7). Since this computation depends greatly on the appropriateness of one-dimensional modeling and the accuracy of such modeling is difficult to estimate, comparison of such a computation with experimental data can hardly establish the capability of the computer program. On the other hand, the finite-difference program was applied across the normal injection region even though there was a limitation due to the parabolic flow assumption (ref. 10). It was later found that such a computation could yield inconsistent results because of the presence of flow recirculation. By using the near-field experimental measurements of reference 9 as input data, the same program was recently applied to the flow field downstream of the injection and the recirculating regions (ref. 11). Because of the insufficiently detailed initial data, only qualitative agreement between the computation and experiment was obtained. Therefore, to evaluate and establish the three-dimensional capabilities of the present computer programs, well-designed experiments are required which provide detailed flow-field surveys at several stations in a supersonic combustor.

It is well recognized that there are many technical difficulties associated with experimental measurements in the supersonic turbulent reacting flow fields of a combustor. Because of the highly turbulent, high-temperature environment, the acquisition of meaningful data is extremely difficult. To alleviate the difficulties associated with high temperature, a three-dimensional cold (nonreacting) flow experiment was performed to study the mixing of helium jets with the supersonic airstream in a rectangular duct. Surveys of the flow field were made at two stations downstream of the injectors, one close to the injectors and the other further downstream. The flow surveys at the upstream station were then used as initial data in both computer programs. The surveys at the downstream station provided an experimental comparison to assess the relative accuracies and computational efficiencies of the computer programs.

The mathematical foundations and numerical schemes of the two computer programs are presented in the first section. Details from earlier work (refs. 1 to 4) have been collected and expanded to provide a convenient comparison of the theories. The three-dimensional mixing experiment is then described relative to test conditions, procedure, data acquisition, and data reduction. Applications of the two computer programs to the experiment are

presented, and comparisons of flow-field quantities are made between the two computations and between the computations and the experiment. Finally, the capabilities of the two programs to compute three-dimensional mixing flow fields are discussed and conclusions are drawn.

SYMBOLS

A	duct cross-sectional area
A_C	computational cross-sectional area
A_N, A_S, A_E, A_W B	coefficients in difference equation (5)
$a(1), a(2), a(3)$	boundary-condition coefficients
$a(1)'$	$= a(1)/a(2)$
$a(3)'$	$= a(3)/a(2)$
a, b, c	functional coefficients
C_1, C_2, C_D, C_k	empirical constants
D	Van Driest damping factor
f	mass fraction; function of dependent or independent variables
g	function of dependent or independent variables
H	total enthalpy
h	static enthalpy
K	general diffusion coefficient
k	turbulence kinetic energy
L, ℓ	differential operators
l_m	mixing length
M	Mach number
\dot{m}	mass flow rate
N_{Pr}	Prandtl number
n_y, n_z	unit normal to y- and z-direction, respectively

P	node point
p	pressure
Q	nodal value vector of dependent variable
q	general dependent flow variable
R	solution domain
∂R	solution domain boundary
R_m	mth finite-element subdomain
∂R_m	mth subdomain boundary
S	source term; surface area
T	temperature
u, v, w	velocity component in x-, y-, and z-direction, respectively
V	volume
W	weighting function
x, y, z	rectangular coordinates
Γ	exchange coefficient
γ	ratio of specific heats
δ_b	boundary-layer thickness
δ_m	mixing-layer thickness
ϵ	turbulence dissipation energy rate
η_m	mixing efficiency
κ	coefficient in equation (7a)
λ	algebraic multiplier; empirical constant
μ	viscosity
ν	kinematic viscosity
ρ	density
τ	shear stress

Φ, Ψ general functions

ϕ space functional

Subscripts:

A air

av average

eff effective

He helium

I injectant

ℓ laminar

m finite-element index

n node index

T total

t turbulent

w wall

Superscripts:

α species α

*

approximate solution

- restrained to boundary of computational domain

DESCRIPTION OF NUMERICAL METHODS

In this section the theoretical bases and numerical schemes of the finite-difference (SHIP) and finite-element (COMOC) computer programs are described. Both programs are developed on the basis of an Eulerian formulation in a rectangular coordinate system (x , y , and z) with the x -axis in the main flow direction. The mean flow velocity components (u , v , and w), pressure (p), total enthalpy (H), and mass fraction (f) of a three-dimensional turbulent mixing flow field are governed approximately by the Navier-Stokes equations together with a species equation. Both programs can consider flow with or without chemical reactions. Moreover, the flow is assumed to be composed of perfect gases with specific heats that are functions of temperature and species.

The effect of turbulence is introduced by replacing the laminar viscosity (μ_ℓ) or the laminar exchange coefficient by an effective viscosity

($\mu_{eff} = \mu_t + \mu_0$) or the corresponding effective exchange coefficient. The turbulent viscosity (μ_t) is determined by means of a turbulence model. In the two computer programs, different turbulence models are used at the present time and they will be discussed separately.

A parabolic flow assumption is used in both programs to simplify their formulations. Physically, this assumption is valid for a flow when there exists a predominant flow direction, when the diffusions of mass, momentum, energy, etc., in this direction are negligible compared with the corresponding convections, and when the downstream pressure has little effect on the upstream flow field. Mathematically, the set of governing equations reduces to a system of parabolic-type equations. Numerically, these equations can be solved in succeeding cross-stream (y-z) planes progressing in the main flow direction. Thus, a three-dimensional problem requires only two-dimensional computer storage, and computer time and storage are greatly reduced. However, because of the parabolic flow assumption, the range of application of the programs is also limited accordingly.

The different features of two programs are described separately in the following discussion.

Finite-Difference Computer Program (SHIP)

The flow field considered in the finite-difference computer program (SHIP) is defined by a rectangular parallelepiped. Any of the four lateral boundaries can be a free, symmetry, or wall surface; for walls, the boundaries are allowed to expand or contract smoothly in the main flow direction. The main flow can be either subsonic or supersonic.

The governing equations for three-dimensional parabolic flow can be written as follows (see also ref. 11):

Continuity

$$\frac{\partial}{\partial x}(\rho u) + \frac{\partial}{\partial y}(\rho v) + \frac{\partial}{\partial z}(\rho w) = 0 \quad (1a)$$

x-momentum

$$\frac{\partial}{\partial x}(\rho u^2) + \frac{\partial}{\partial y}(\rho v u) + \frac{\partial}{\partial z}(\rho w u) = -\frac{\partial p}{\partial x} + \frac{\partial}{\partial y}\left(\mu_{eff} \frac{\partial u}{\partial y}\right) + \frac{\partial}{\partial z}\left(\mu_{eff} \frac{\partial u}{\partial z}\right) \quad (1b)$$

y-momentum

$$\frac{\partial}{\partial x}(\rho u v) + \frac{\partial}{\partial y}(\rho v^2) + \frac{\partial}{\partial z}(\rho w v) = -\frac{\partial p}{\partial y} + \frac{\partial}{\partial y}\left[\frac{2}{3}\mu_{eff}\left(2\frac{\partial v}{\partial y} - \frac{\partial w}{\partial z}\right)\right] + \frac{\partial}{\partial z}\left[\mu_{eff}\left(\frac{\partial v}{\partial z} + \frac{\partial w}{\partial y}\right)\right] \quad (1c)$$

z-momentum

$$\frac{\partial}{\partial x}(\rho uw) + \frac{\partial}{\partial y}(\rho vw) + \frac{\partial}{\partial z}(\rho w^2) = -\frac{\partial p}{\partial z} + \frac{\partial}{\partial y} \left[\mu_{eff} \left(\frac{\partial v}{\partial z} + \frac{\partial w}{\partial y} \right) \right] + \frac{\partial}{\partial z} \left[\frac{2}{3} \mu_{eff} \left(2 \frac{\partial w}{\partial z} - \frac{\partial v}{\partial y} \right) \right] \quad (1d)$$

Energy

$$\begin{aligned} \frac{\partial}{\partial x}(\rho uH) + \frac{\partial}{\partial y}(\rho vH) + \frac{\partial}{\partial z}(\rho wH) &= \frac{\partial}{\partial y} \left(\frac{\mu_{eff}}{N_{Pr,eff,H}} \frac{\partial H}{\partial y} \right) + \frac{\partial}{\partial z} \left(\frac{\mu_{eff}}{N_{Pr,eff,H}} \frac{\partial H}{\partial z} \right) \\ &+ \frac{\partial}{\partial y} \left[\frac{\mu_{eff}}{N_{Pr,eff,H}} (N_{Pr,eff,H} - 1) \frac{\partial}{\partial y} \left(\frac{u^2 + v^2 + w^2}{2} \right) \right] \\ &+ \frac{\partial}{\partial z} \left[\frac{\mu_{eff}}{N_{Pr,eff,H}} (N_{Pr,eff,H} - 1) \frac{\partial}{\partial z} \left(\frac{u^2 + v^2 + w^2}{2} \right) \right] \\ &+ \mu_{eff} \left[\left(\frac{\partial v}{\partial y} \right)^2 + \left(\frac{\partial w}{\partial z} \right)^2 + 2 \frac{\partial v}{\partial z} \frac{\partial w}{\partial y} \right] \end{aligned} \quad (1e)$$

Species¹

$$\frac{\partial}{\partial x}(\rho uf) + \frac{\partial}{\partial y}(\rho vf) + \frac{\partial}{\partial z}(\rho wf) = \frac{\partial}{\partial y} \left(\frac{\mu_{eff}}{N_{Pr,eff,f}} \frac{\partial f}{\partial y} \right) + \frac{\partial}{\partial z} \left(\frac{\mu_{eff}}{N_{Pr,eff,f}} \frac{\partial f}{\partial z} \right) \quad (1f)$$

Here, $N_{Pr,eff,H}$ and $N_{Pr,eff,f}$ are the effective Prandtl numbers for total enthalpy and mass fraction, respectively. The general effective exchange coefficient Γ is expressed in the following form,

$$\Gamma \equiv \frac{\mu_{eff}}{N_{Pr,eff}} = \frac{\mu_l}{N_{Pr,l}} + \frac{\mu_t}{N_{Pr,t}} \quad (2)$$

with $N_{Pr,l}$ and $N_{Pr,t}$ being the laminar and turbulent Prandtl numbers, respectively. Since $N_{Pr,l}$ and $N_{Pr,t}$ are of the order of unity and $\mu_t \gg \mu_l$ in fully developed turbulent flow, $\Gamma \sim \mu_t/N_{Pr,t}$. Note that some terms in the set of equations (1) which were omitted in reference 1 have been included for completeness, and the finite-difference program has also been updated accordingly.

¹Only one differential equation for the mass fraction is solved; remaining species are calculated on the basis of stoichiometric considerations.

A "k-ε" two-equation turbulence model is used (ref. 1). From a dimensional analysis, the turbulent viscosity μ_t is proportional to the flow density, a turbulence velocity scale (e.g., the square root of the turbulence kinetic energy k), and a turbulence length scale l . In high Reynolds number flows, $l \sim k^{3/2}/\epsilon$ with ϵ being the turbulence dissipation energy rate; hence, $\mu_t = C_D \rho k^2/\epsilon$ where C_D is an empirical constant and k and ϵ are governed by a set of transport equations. Under the parabolic flow assumption, these transport equations are

$$\begin{aligned} \frac{\partial}{\partial x}(\rho u k) + \frac{\partial}{\partial y}(\rho v k) + \frac{\partial}{\partial z}(\rho w k) &= \frac{\partial}{\partial y} \left(\frac{\mu_{\text{eff}}}{N_{\text{Pr,eff},k}} \frac{\partial k}{\partial y} \right) + \frac{\partial}{\partial z} \left(\frac{\mu_{\text{eff}}}{N_{\text{Pr,eff},k}} \frac{\partial k}{\partial z} \right) \\ &+ \mu_t \left\{ 2 \left[\left(\frac{\partial v}{\partial y} \right)^2 + \left(\frac{\partial w}{\partial z} \right)^2 \right] + \left(\frac{\partial u}{\partial y} \right)^2 + \left(\frac{\partial u}{\partial z} \right)^2 \right. \\ &\left. + \left(\frac{\partial v}{\partial z} + \frac{\partial w}{\partial y} \right)^2 \right\} - \rho \epsilon \end{aligned} \quad (3a)$$

$$\begin{aligned} \frac{\partial}{\partial x}(\rho u \epsilon) + \frac{\partial}{\partial y}(\rho v \epsilon) + \frac{\partial}{\partial z}(\rho w \epsilon) &= \frac{\partial}{\partial y} \left(\frac{\mu_{\text{eff}}}{N_{\text{Pr,eff},\epsilon}} \frac{\partial \epsilon}{\partial y} \right) + \frac{\partial}{\partial z} \left(\frac{\mu_{\text{eff}}}{N_{\text{Pr,eff},\epsilon}} \frac{\partial \epsilon}{\partial z} \right) \\ &+ C_1 \frac{\epsilon}{k} \mu_t \left\{ 2 \left[\left(\frac{\partial v}{\partial y} \right)^2 + \left(\frac{\partial w}{\partial z} \right)^2 \right] + \left(\frac{\partial u}{\partial y} \right)^2 \right. \\ &\left. + \left(\frac{\partial u}{\partial z} \right)^2 + \left(\frac{\partial v}{\partial z} + \frac{\partial w}{\partial y} \right)^2 \right\} - C_2 \frac{\rho \epsilon^2}{k} \end{aligned} \quad (3b)$$

where C_1 and C_2 are empirical constants associated with the k-ε two-equation turbulence model.

The set of simplified parabolic flow equations can be cast in a conservative form:

$$\frac{\partial}{\partial x}(\rho u q) + \frac{\partial}{\partial y} \left(\rho v q - \Gamma_q \frac{\partial q}{\partial y} \right) + \frac{\partial}{\partial z} \left(\rho w q - \Gamma_q \frac{\partial q}{\partial z} \right) = S_q \quad (4)$$

where q is a general dependent variable and Γ_q and S_q are the exchange coefficient and source term, respectively, associated with the dependent variable q . When q equals 1 , u , v , w , H , f , k , or ϵ , equation (4) corresponds to the equations for continuity, the three components of momentum, energy, species, turbulence kinetic energy, or turbulence dissipation energy rate. Numerical computation is based on a finite-difference formulation of equation (4). A "staggered" grid system is used in the cross-stream (y - z) plane and variable grid spacings are allowed. Figure 1 shows such a staggered grid system. In the figure, P indicates an arbitrary node point; its four neighboring points are denoted by E , W , N , and S for east, west, north, and south. All variables at an arbitrary node are stored at the location P except the transverse velocity components v and w : v is stored at the midpoint between W and P , and w is stored at the midpoint between S and P , as shown by the arrows in figure 1. Thus, control volumes at each node point are different for v and w compared with those for the other dependent variables. By taking volume integrations of equation (4) over respective control volumes, a set of difference equations can be obtained.

The volume integrations of the terms $\frac{\partial}{\partial x}(\rho u q)$ and S_q in equation (4)

are performed by assuming that the values of q , ρ , and u at a node point P are constant over the entire control volume. The term $\partial/\partial x$ contains the difference of values of stations x and $x + \Delta x$. The volume integrations of the other two terms in equation (4) give rise to the surface integrals of the convective and diffusive fluxes across the boundaries of the control volume. Proper representation of these terms is essential to the convergence of the numerical computation. To provide numerical convergence and accuracy, a "hybrid" scheme is used (ref. 12) which is a combination of central and upwind differences. When the integrations of various terms in equation (4) are expressed in the manner just described, the general form of a difference equation at an arbitrary node point P is written in the following form:

$$q_P = A_N q_N + A_S q_S + A_E q_E + A_W q_W + B \quad (5)$$

where the values of the q 's pertain to station $x + \Delta x$ and the values of the A 's and B pertain to station x . The subscripts N , S , E , and W denote the neighboring north, south, east, and west nodes (fig. 1).

The set of difference equations (eq. (5)) together with other auxiliary relations are solved by a so-called SIMPLE (semi-implicit method for pressure linked equations) procedure (ref. 1). Although the governing equations are highly nonlinear, an economical noniterative marching procedure in the streamwise direction is followed. The three velocity components are solved first from their respective equations (i.e., $q = u$, v , and w) in terms of a guessed pressure field. Then a pressure correction is obtained from an equation derived from the continuity equation and having a form similar to equation (5). After the pressure field and the three velocity components have been corrected, the difference equations for H , f , k , and ϵ are solved sequentially. Temperature, density, and mass fraction for each species and other auxiliary variables are determined noniteratively.

In the finite-difference program, the boundary conditions are specified by the values of appropriate fluxes across the boundaries. For a free-stream or symmetry boundary, fluxes are set automatically to zero. To avoid using a large number of grid points for calculating large gradients near a solid wall, the boundary conditions are described by the law of the wall at near-boundary grid points (ref. 13). Once the boundary conditions are properly specified, each of the difference equations (eq. (5)) is solved in a line-by-line iterative fashion in the cross-stream (y-z) plane by the successive application of a standard tridiagonal matrix algorithm in the y- and z-directions.

The accuracy of the computation is determined by examining the conservation of mass flow in each cross-stream plane and the mass residue at each node point; both the mass residue at each node point and the mass-flow imbalance in the entire cross-stream plane are expected to be small. The accuracy may be improved by increasing the number of grid points in the cross-stream plane, increasing the number of iterations for solving difference equations, or using smaller forward steps in the streamwise direction.

Finite-Element Computer Program (COMOC)

The finite-element computer program (COMOC) considers flow in a constant-area rectangular duct with arbitrary boundary conditions on either the four duct walls, symmetry planes lying within the duct, or any combination of these boundaries. The flow can be either subsonic or supersonic, with the only restriction being that streamwise diffusion is negligible so that a parabolic character is maintained.

Either a mixing-length or a k- ϵ two-equation turbulence model (ref. 2) is available in COMOC to calculate the effective turbulent viscosity. The k- ϵ model requires solving two partial differential equations in addition to the governing equations. Even though the increase in the number of equations is small, the equations for the turbulence kinetic energy and dissipation energy rate are quite "stiff" for the COMOC integration algorithm. Although an effort is currently underway to streamline the integration technique, the present work used the turbulence model based on mixing-length theory (ref. 2) to improve computational efficiency for the large domains being considered.

The parabolic Navier-Stokes, energy, and species equations describing the flow are given in reference 2. In the notation of the present paper, they are

Continuity

$$\frac{\partial}{\partial x}(\rho u) + \frac{\partial}{\partial y}(\rho v) + \frac{\partial}{\partial z}(\rho w) = 0 \quad (6a)$$

x-momentum

$$\rho \left(u \frac{\partial u}{\partial x} + v \frac{\partial u}{\partial y} + w \frac{\partial u}{\partial z} \right) = - \frac{\partial p}{\partial x} + \frac{\partial}{\partial y} \left(\mu_{\text{eff}} \frac{\partial u}{\partial y} \right) + \frac{\partial}{\partial z} \left(\mu_{\text{eff}} \frac{\partial u}{\partial z} \right) \quad (6b)$$

y-momentum

$$\rho \left(u \frac{\partial v}{\partial x} + v \frac{\partial v}{\partial y} + w \frac{\partial v}{\partial z} \right) = - \frac{\partial p}{\partial y} + \frac{\partial}{\partial y} \left(\mu_{\text{eff}} \frac{\partial v}{\partial y} \right) + \frac{\partial}{\partial z} \left(\mu_{\text{eff}} \frac{\partial v}{\partial z} \right) \quad (6c)$$

z-momentum

$$\rho \left(u \frac{\partial w}{\partial x} + v \frac{\partial w}{\partial y} + w \frac{\partial w}{\partial z} \right) = - \frac{\partial p}{\partial z} + \frac{\partial}{\partial y} \left(\mu_{\text{eff}} \frac{\partial w}{\partial y} \right) + \frac{\partial}{\partial z} \left(\mu_{\text{eff}} \frac{\partial w}{\partial z} \right) \quad (6d)$$

Energy

$$\begin{aligned} \rho \left(u \frac{\partial H}{\partial x} + v \frac{\partial H}{\partial y} + w \frac{\partial H}{\partial z} \right) = & \frac{\partial}{\partial y} \left(\frac{\mu_{\text{eff}}}{N_{\text{Pr,eff,H}}} \frac{\partial H}{\partial y} \right) + \frac{\partial}{\partial z} \left(\frac{\mu_{\text{eff}}}{N_{\text{Pr,eff,H}}} \frac{\partial H}{\partial z} \right) \\ & - \frac{\partial}{\partial y} \left[\frac{1 - N_{\text{Pr,eff,H}}}{N_{\text{Pr,eff,H}}} \frac{\mu_{\text{eff}}}{2} \frac{\partial}{\partial y} (u^2 + v^2 + w^2) \right] \\ & - \frac{\partial}{\partial z} \left[\frac{1 - N_{\text{Pr,eff,H}}}{N_{\text{Pr,eff,H}}} \frac{\mu_{\text{eff}}}{2} \frac{\partial}{\partial z} (u^2 + v^2 + w^2) \right] \\ & - \frac{\partial}{\partial y} \left(\frac{N_{\text{Pr,eff,f}} - N_{\text{Pr,eff,H}}}{N_{\text{Pr,eff,f}} N_{\text{Pr,eff,H}}} \mu_{\text{eff}} \sum_{\alpha} h^{\alpha} \frac{\partial f^{\alpha}}{\partial y} \right) \\ & - \frac{\partial}{\partial z} \left(\frac{N_{\text{Pr,eff,f}} - N_{\text{Pr,eff,H}}}{N_{\text{Pr,eff,f}} N_{\text{Pr,eff,H}}} \mu_{\text{eff}} \sum_{\alpha} h^{\alpha} \frac{\partial f^{\alpha}}{\partial z} \right) \end{aligned} \quad (6e)$$

Species

$$\rho \left(u \frac{\partial f^{\alpha}}{\partial x} + v \frac{\partial f^{\alpha}}{\partial y} + w \frac{\partial f^{\alpha}}{\partial z} \right) = \frac{\partial}{\partial y} \left(\frac{\mu_{\text{eff}}}{N_{\text{Pr,eff,f}}} \frac{\partial f^{\alpha}}{\partial y} \right) + \frac{\partial}{\partial z} \left(\frac{\mu_{\text{eff}}}{N_{\text{Pr,eff,f}}} \frac{\partial f^{\alpha}}{\partial z} \right) + S^{\alpha} \quad (6f)$$

where f^{α} , h^{α} , and S^{α} are the mass fraction, static enthalpy, and source term, respectively, of species α (for nonreacting flows, $S^{\alpha} = 0$). The effective Prandtl number for the mass fraction $N_{\text{Pr,eff,f}}$ (the effective Schmidt number) is assumed to be the same for all species. Equations (6b) to (6e) do not form a completely parabolic system because certain cross-derivative shear terms in the y- and z-momentum equations and viscous dissipation terms in the energy equation have not been considered. These terms were assumed to be small in the development of the finite-element program and therefore were dropped. They are cur-

rently being added, however, in a newer version of the program. Equation (6) can be expressed in general form as

$$L(q) = \kappa \left\{ \frac{\partial}{\partial y} \left[K(q) \frac{\partial q}{\partial y} \right] + \frac{\partial}{\partial z} \left[K(q) \frac{\partial q}{\partial z} \right] \right\} + f \left(q, \frac{\partial q}{\partial x}, \frac{\partial q}{\partial y}, \frac{\partial q}{\partial z}, x, y, z \right) - g(q, x) = 0 \quad (7a)$$

with generalized boundary conditions

$$l(q) = a(1)q(x, \bar{y}, \bar{z}) + a(2)K(q) \left[\frac{\partial}{\partial y} q(x, \bar{y}, \bar{z}) n_y + \frac{\partial}{\partial z} q(x, \bar{y}, \bar{z}) n_z \right] - a(3) = 0 \quad (7b)$$

where q is any dependent variable, K is a generalized diffusion coefficient, f and g are functions of the specified variables, and κ , $a(1)$, $a(2)$, and $a(3)$ are specifiable constants. The superscript bar restrains y and z to the boundaries of the computational domain.

A computational domain is defined identically with the duct cross-sectional area at the initial station of the solution domain. This area is then discretized, as shown in figure 2, with triangular finite elements sized by the user with respect to the initial rate of change of the variables q in each element (solution subdomain). The triangles are chosen small for high resolution where the gradients of q are large; they are chosen large for computational economy where the gradients of q are small. This finite-element scheme provides a convenient means of transforming the partial differential equations describing the system into coupled ordinary differential equations that can be more readily solved. Within each triangular element, the variables q are assumed to vary in a linear fashion described by

$$q_m^*(x, y, z) = a_m + b_m y + c_m z \quad (8)$$

where q_m^* is the approximate solution to q in the m th element and a , b , and c define the values of q_m^* at the three corners of the triangle. For subsequent use, equation (8) is more conveniently expressed in vector form as

$$q_m^*(x, y, z) = \{\phi(y, z)\}^T \{Q_m(x)\} \quad (9a)$$

where

$$\{\phi(y, z)\} = \begin{Bmatrix} 1 \\ y \\ z \end{Bmatrix} \quad (9b)$$

$$\{Q_m(x)\} = \begin{Bmatrix} a_m \\ b_m \\ c_m \end{Bmatrix} \quad (9c)$$

and superscript T indicates the transpose of the vector.

To determine the Q 's at each node, which are the solutions sought, the approximate solutions q^* are substituted into the differential equations (eq. (7a)) constrained by boundary conditions (eq. (7b)). If the values of $L(q^*)$ and $\ell(q^*)$, referred to as residuals, can be reduced collectively to zero over the solution subdomain, the approximate solution then approaches the exact solution of equation (7a), as the element size is reduced to zero in the limit.

Values of the residuals are best minimized by integrating over the entire element subdomain with weight W and requiring that the result vanish; that is,

$$\int_{R_m} W L(q_m^*) dV - \lambda \oint_{\partial R_m \cap \partial R} W \ell(q_m^*) dS = 0 \quad (10)$$

This procedure is commonly referred to as the method of weighted residuals. Here, R_m denotes the element subdomain, ∂R_m the subdomain boundary, ∂R the computational domain boundary, and \cap the intersection of these two boundaries. The second integration is performed only when an element lies on the boundaries of the duct cross section being computed. Weighting allows the functional dependence of q^* to be felt throughout the integral domain. The unknown algebraic multiplier λ has been included (ref. 2) for use later in simplifying the equation system.

In order to proceed with equation (10), appropriate weights on L and ℓ must be defined. The Galerkin procedure, applied here, chooses the weights to be identical with ϕ (eq. (9b)). Experience has shown that this procedure yields the most appropriate weighting to equation (10) consistent with the system being solved. Equation (10) then becomes

$$\int_{R_m} \{\phi(y, z)\} L(q_m^*) dV - \lambda \oint_{\partial R_m \cap \partial R} \{\phi(y, z)\} \ell(q_m^*) dS = \{0\} \quad (11)$$

Equation (11) describes the variation of the dependent variables q over each finite element within the computational domain. To describe q over the entire domain, equation (11) with appropriate simplifying modifications (refs. 2, 7, and 14) must be summed (symbol \cup) over all the finite elements. The details of this development are rather involved and are presented in the appendix; the result is

$$\begin{aligned} & \cup \left\{ -K \int_{R_m} \left[\frac{\partial \{\phi\}}{\partial y} K \frac{\partial q_m^*}{\partial y} + \frac{\partial \{\phi\}}{\partial z} K \frac{\partial q_m^*}{\partial z} \right] dV + \int_{R_m} \{\phi\} (f_m^* - g_m^*) dV \right. \\ & \left. - K \oint_{\partial R_m \cap \partial R} \{\phi\} \left(a_m^{(1)'} q_m^* - a_m^{(3)'} \right) dS \right\} = \{0\} \quad (12) \end{aligned}$$

Equation (12) is the basis of the solution algorithm for all dependent variables of the COMOC finite-element computer program. It is applied directly to the three momentum equations, the energy equation, and the species equation. A system of simultaneous first-order ordinary differential equations in the x (streamwise) coordinate direction then results for the dependent variables. These equations are solved at each streamwise station using a predictor-corrector numerical integration scheme (ref. 7). The value of each dependent variable is predicted at the first downstream station (first step) using a simple Euler scheme based on the variable's streamwise derivative at the initial station. Predictions at subsequent steps are obtained from the predictor formula. At each step, the predictions are then corrected by the more accurate corrector formula. The scheme is absolutely stable and has an error of the order of the square of the step size in the streamwise direction. The step size is adjusted with respect to a maximum relative truncation error and is continually increased up to this limit while downstream stepping to reduce the required computer time. When the error limit is exceeded, the preceding step size to a new station is reduced and the values of the dependent variables at the new station are recalculated.

As the solution marches downstream, continuity is enforced by insuring that mass is conserved at each streamwise station. Conservation is guaranteed by correcting the streamwise pressure gradient at each station, so that the computational cross-sectional area of the flow A_C matches as closely as possible the actual cross-sectional area A of the duct. This computational cross-sectional area is directly related to the total mass flow rate \dot{m} by

$$A_C = \frac{\dot{m}}{\left(\sum_{n=1}^N \rho_n u_n \right) / N} \quad (13)$$

where ρ_n and u_n are local values of density and streamwise velocity at each of the N nodes forming the finite-element grid. The change in computational area necessary to match the actual area is then,

$$\frac{dA_C}{dx} \approx \frac{A - A_C}{\Delta x} \quad (14)$$

where Δx is the step size. The derivative dA_C/dx is directly related to the streamwise pressure gradient dp/dx by (ref. 13)

$$\frac{dp}{\partial x} = \frac{-\tau_{av} + \frac{u\dot{m}}{A^2} \frac{dA_C}{dx} - \frac{u\dot{m}}{AT_{av}} \frac{dT_{av}}{dx}}{1 - \gamma M_{av}^2} \quad (15)$$

where T_{av} is the average wall shear over the step, T_{av} is the area-averaged temperature, M_{av} is the area-averaged Mach number over the cross section, and γ is the ratio of specific heats. COMOC currently considers only this stream-wise variation of pressure. However, the capability to calculate both transverse pressure fields is now being implemented in the program.

Specifiable boundary conditions in COMOC are of three basic types. The symmetry (vanishing gradient) boundary condition, where the normal derivative of any dependent variable vanishes, is the default boundary condition in COMOC (see appendix). Alternately, the value of dependent variables can be held at its initial value along any boundary. Finally, a finite value of the normal derivative of a dependent variable along any boundary can be specified. This "derivative boundary condition" is useful in turbulent flows and will be described more fully later.

EXPERIMENTAL TEST CASE

Apparatus and Test Conditions

A three-dimensional turbulent mixing experiment has been conducted to provide detailed data for comparison of the two computer programs. The experiment involves the mixing of helium jets with a supersonic airstream in a rectangular combustor duct. A sketch of the injector strut and combustor duct is presented in figure 3. The combustor duct has a constant cross section 0.0381 m by 0.17 m. The first section of the duct contains the injection strut, which is centered in the shorter dimension and spans the longer dimension of the duct cross section. The combustor duct incorporates hinge joints at the 0.309-m station for making adjustments to the combustor geometry. Flow to the combustor duct is provided by a rectangular Mach 2.99 nozzle at a total temperature of 294 K and a total pressure of 1.6 MPa (see table I).

Details of the injector strut are presented in figure 4. Previous tests of this strut, reported in reference 15, were performed with an area ratio of 2 over the aft 0.479-m section of the combustor. This strut was designed for combustion tests, and therefore, the leading edge has provisions for water cooling. The strut consists of a 6° half-angle wedge with a maximum thickness of 0.01 m and a 0.0016-m-radius leading edge. The aft body has constant thickness and a blunt base. Five equally spaced fuel injectors located on the base divide the flow into five nearly square (0.0340 m by 0.0381 m) regions. Four of the injectors are 10° half-angle conical nozzles which operate slightly overexpanded. The other injector has two sonic jets directed toward each other with a combined jet cross-sectional area equal to the throat area of the other jets. The injectant is supplied through the passages labeled "Helium" in figure 4. As listed in table I, helium is injected at a total temperature of 294 K and a total pressure of 3.27 or 3.79 MPa, which produce a bulk helium-to-air mass-flow ratio of 0.024 or 0.027, respectively.

Instrumentation

Measurements included total injectant flow rate, total pressure and temperature of air and injectant, combustor wall pressures, and instream surveys of static pressure, pitot pressure, and gas composition. Comparisons between the injectant flow rate measured by a venturi in the helium supply line and the flow rate calculated by one-dimensional isentropic compressible flow relations at the injector throat show that the bulk discharge coefficient for the five jets was approximately 0.81. Combustor wall pressures were measured along the entire length of the upper wall, primarily on the wall center line. Instream flow surveys of pitot pressure and gas composition were made with a 13-probe rake which incorporated internal expansion pitot probes, as illustrated in figure 5(a). The probes were mounted at a center-to-center spacing of 0.00635 m. The pitot probe utilizes an internal expansion design to aid in collecting accurate gas samples by reducing or eliminating tip spillage. All 13 pitot pressures were recorded simultaneously; then 13 gas sample bottles were filled. These bottles were analyzed on a process gas chromatograph between survey runs. Instream static pressure was obtained with a probe rake incorporating the static probe tips illustrated in figure 5(b). This static probe tip is less susceptible to errors from misalignment with the flow direction than conventional static probes (ref. 16). Static tips were located on the rake at a center-to-center spacing of 0.0127 m (double the pitot spacing) to eliminate flow interference between the tips. Thus, two passes were required to complete static pressure flow mapping at each survey station.

The metered air and helium mass flow rates are estimated to have an accuracy within ± 2 percent. Accuracies of pitot pressure, static pressure, and gas concentration are estimated to be within ± 2 percent, ± 4 percent, and ± 1 percent, respectively. Another source of error in the data acquisition is repeatability of the test conditions for different surveys. The air and helium mass flows varied by about ± 5 percent from test to test, so the measured pitot and static pressures were adjusted by the ratio of the actual air total pressure to mean air total pressure.

Experimental Results

Flow-field surveys were made at two streamwise stations, $x = 0.0421$ m and $x = 0.7369$ m downstream from the base of the injection strut. At the upstream station ($x = 0.0421$ m), the surveys were concentrated in the region of the flow occupied by the injectant. At the downstream station ($x = 0.7369$ m), the entire flow field was surveyed. Measured pitot and static pressures and gas concentrations were reduced to generate tabulated data, flow-field profiles, and contour plots of various flow properties.

Helium mass fraction contours for the entire duct cross section at the downstream station ($x = 0.7369$ m) are presented in figure 6. Corresponding to the five injectors are five almost equally spaced mixing regions with distinct boundaries. Dashed vertical lines, located midway between the projected locations of the jet center lines, emphasize the mixing regions. Integrations of air and helium mass flows in each of the five mixing regions show that the mass flows are almost the same in each region, although at the downstream station the

jets have already merged with their neighboring jets. As shown in figure 6, the flow field downstream of the crossed injector (second from left) is more uniform than those of the other parallel injectors. All four parallel-injection mixing regions are quite similar with the exception of slight shifts from the projected injection location (solid symbols in fig. 6). The center jet region was surveyed more extensively than the other jet regions. Therefore, the center jet was chosen as a typical flow field to be computed by the two computer programs.

The reduced survey data in the center jet region for the streamwise velocity, static pressure, temperature, and helium mass fraction are tabulated in tables II and III for the upstream ($x = 0.0421$ m) and the downstream ($x = 0.7369$ m) stations, respectively. These data have been adjusted to the bulk flow pressures listed in table I and were reduced by assuming constant total temperature. In the following discussions, detailed surveys of the center mixing region are presented.

Figure 7 illustrates the center jet mixing region relative to the upstream projection of the strut and center fuel injector. The top and bottom boundaries are formed by the combustor wall, and the side boundaries by the center planes between adjacent jets. Vertical locations of the probe tips and horizontal locations of the rake at the upstream survey station ($x = 0.0421$ m) are represented by the tick marks on the respective boundaries. Thus, the intersections of horizontal and vertical lines through the tick marks represent the locations of survey points.

Figures 8(a) and 8(b) present the helium mass fraction contours at the upstream and downstream survey stations, respectively. At the upstream survey station, the five individual jets are still separate, each having spread over only about half of the mixing-region width. At the downstream station, the flow is nearly stratified in the vertical direction because of merging between adjacent jets. The maximum helium mass fraction measured at the upstream station is 0.36; at the downstream station, it is 0.035.

Helium mass flow rate contours are very similar in appearance to the mass fraction contours of figure 8 and are not presented. Helium mass flow rate contours were numerically integrated and the result was nondimensionalized by the metered mass flow rate from one jet. The result, presented in figure 8 by the symbol \dot{m}_{He} , shows a 16- and 10-percent deficiency in helium mass-flow measurement at the upstream and downstream stations, respectively. This is consistent with previous cold mixing studies where surveys taken close to the jet in regions of sharp concentration and velocity gradients exhibit significant injectant mass-flow deficiencies. A 12-percent deficiency in air mass-flow measurement was observed by integrations of the air mass flow rate contours.

Velocity contours are presented in figures 9(a) and 9(b) at the upstream and downstream survey stations, respectively. The helium jet exit velocity is 1539 m/sec, and the air velocity ahead of the strut is 617 m/sec. At the upstream station surveyed, the jet has a much higher velocity than the surrounding air. The peak velocity in the jet flow is about 1100 m/sec; outside the central jet region, the velocity is in the range of 366 to 488 m/sec. This air velocity deficiency from 617 m/sec ahead of the strut is indicative of the

pressure loss caused by strut-induced shock waves. At the downstream station, the velocity is more uniform and has decayed as a result of viscous losses in the duct. The velocity ranges from 335 m/sec near the wall to 457 m/sec at the combustor center line and appears similar to turbulent-boundary-layer-type flow.

Static pressure contours are presented in figure 10 for the two survey stations. At the upstream station (fig. 10(a)), pressure in the region of the injectant is lower than in the surrounding flow. The pressure increases slightly toward the wall, as expected, because of the wave structure produced by the strut. At the downstream station (fig. 10(b)), the static pressure is more random but at a higher value because of viscous losses in the duct.

Static temperature contours, reduced from the survey data by assuming constant total temperature, are presented in figure 11 for the two survey stations. Because the total temperature is assumed to be constant, these surveys are similar to the velocity contours. At the upstream station (fig. 11(a)), the minimum static temperature at the center of the helium jet is about 139 K. The maximum static temperature adjacent to the wall is about 256 K. At the downstream station (fig. 11(b)), the minimum and maximum values are about 194 K and 244 K.

NUMERICAL COMPUTATIONS

In this section, the finite-difference and finite-element computer programs are applied to the helium mixing experiment described in the previous section. Because of the symmetric nature of the flow field downstream of each jet, only the flow field downstream of the central jet is considered in the present calculation. In order to take full advantage of the maximum storage in the computer programs, the finite-difference program computed only half of the central jet (region ABCDEFA in fig. 12), and the finite-element program computed one-quarter of the central jet (region ABCFA in fig. 12). The approximate symmetry of the central jet flow field allowed this reduction in the computational domains. Since for comparison of the two programs the two computations must be based on the same set of initial conditions, the acquisition of the initial conditions will be described first. Then, the application of two programs to the problem with respect to their grid arrangements, initial and boundary conditions, initial estimates of turbulence kinetic energy and dissipation rate, and computer time and storage required is described. Finally, computational results of both computer programs are presented for comparison with each other and with the experimental data. The essential differences between the two computations from SHIP and COMOC are presented in table IV.

Initial Data

As described in the section, "Experimental Test Case," the measurements of static and pitot pressures and helium mass fraction were made at two streamwise stations. From these measurements, the streamwise velocity, temperature, pressure, air and helium mass fractions, and density of the mixture were deduced. In the center jet region, however, there are only 9×7 points of measurement, too coarse to represent the details of the initial conditions for

the computations. Therefore, the experimental data (streamwise velocity, temperature, pressure, and helium mass fraction) were interpolated according to the desired grid arrangement in the initial cross-stream plane by using cubic-spline interpolation. Initial profiles of streamwise velocity, temperature, pressure, and helium mass fraction from the center plane ($z = 0$) to the duct wall ($z = 0.01905$ m) at several stations along the y -axis are shown in figure 13. The symbols are the experimental data and the lines are the profiles interpolated from these data. Note that at the initial station, there were shocks; however, because of the limited measured data, the positions and intensities of these shocks cannot be easily determined. Therefore, the initial profiles of the interpolated flow variables show smooth variations over the entire cross-stream plane. It is believed that in the parabolic flow field, the error due to such approximations does not produce significant downstream effects since any discontinuities will be diffused (smoothed out) within a short distance downstream.

Finite-Difference Program

In the finite-difference computer program (SHIP), the initial conditions required are the three velocity components, temperature, pressure, and mass fraction of all species. From these flow variables, the values of density, total enthalpy, and turbulence kinetic energy and dissipation rate can be either calculated or estimated. In the present computation, the two lateral velocity components were taken to be initially zero, because they were not measured and were assumed to be small compared with the streamwise velocity component. The helium mass flow and the total mass flow computed from the initial profiles are 0.01193 kg/sec and 0.5975 kg/sec, respectively, whereas they were 0.01425 kg/sec and 0.5960 kg/sec in the experiment.

The initial turbulence kinetic energy and dissipation rate also were not measured; hence, they must be estimated. One method, suggested in reference 17, is to use an estimated shear-stress profile. For a two-dimensional subsonic turbulent boundary layer or turbulent mixing layer of homogeneous medium, it was found (ref. 11) that an estimate based on the Prandtl mixing-length hypothesis is adequate. For a turbulent mixing layer of different mediums, however, the mixing length seems to depend on the variation of density (ref. 11). Since there are no rigorous conventional methods available to determine the turbulence kinetic energy and dissipation rate from the local flow variables in a three-dimensional flow, the following estimate was used in the present finite-difference computation.

It was assumed that the turbulence kinetic energy at the initial station was composed of two parts, one due to the background value and the other due to the shear stress, as suggested in reference 17 for two-dimensional flows. The background turbulence kinetic energy k_0 is defined as a fraction of the mean flow kinetic energy; that is, in the present computation, $k_0 = (5.56 \times 10^{-5}) u_{av}^2$ with u_{av} being the average velocity of the airstream. The turbulence kinetic energy due to the shear stress depends on the local maximum velocity gradient $\partial u / \partial s$ ($\partial u / \partial s$ is the greater value of $\partial u / \partial y$ and $\partial u / \partial z$) and a mixing length l_m . For flow near the duct wall, the mixing length

in the conventional turbulent boundary layer was used; near the jet, the mixing length in the axisymmetric mixing layer was assumed. Thus,

$$k = k_0 + \frac{l_m^2 \left| \frac{\partial u}{\partial s} \right|^2}{C_D^{1/2}} \quad (16)$$

In the present coordinate system (fig. 12), for flow near the duct wall, $z \geq 0.01905 - 0.09\delta_b/0.435$ with $\delta_b = 0.007$ m being the wall boundary-layer thickness. In this region, l_m is (ref. 11)

$$l_m = 0.435(0.01905 - z) \left\{ 1 - \exp \left[- \frac{(0.01905 - z)(\tau\rho)^{1/2}}{26\mu_l} \right] \right\} \quad (17a)$$

Outside of this region (i.e., $z < 0.01905 - 0.09\delta_b/0.435$),

$$l_m = 0.11\delta_m \quad (17b)$$

with $\delta_m = 0.005$ m being the mixing-layer thickness. Similarly, the turbulence dissipation rate and the turbulent viscosity were assumed to be

$$\epsilon = \frac{k_0^{3/2}}{0.625\delta_m} + l_m^2 \left| \frac{\partial u}{\partial s} \right|^3 \quad (18)$$

and

$$\mu_t = \frac{C_D \rho k_0^2}{0.625\delta_m} + \rho l_m^2 \left| \frac{\partial u}{\partial s} \right| \quad (19)$$

No-flux boundary conditions were specified at the three symmetric boundaries; on the duct wall, the velocity was zero, the temperature was constant, and heat transfer was allowed.

In the finite-difference computation, nonuniform grid spacings were chosen; 11×30 grid points were used in the y - z plane. The computation was performed from the initial station ($x = 0.0421$ m downstream from the strut) to a downstream station ($x = 0.7369$ m) with the empirical constants $C_1 = 1.44$, $C_2 = 1.92$, $C_D = 0.09$, laminar Prandtl number $N_{Pr,l} = 0.7$, and turbulent Prandtl numbers $N_{Pr,t,q} = 1.0$ for $q = u, v, w, k$, $N_{Pr,t,\epsilon} = 1.3$, $N_{Pr,t,H} = 0.9$, and $N_{Pr,t,f} = 0.7$. A total 690 variable-sized streamwise forward steps were taken. Total computer time was 261 sec on the Control Data CYBER 175 computer system; the total computer storage used was 77400g words. The accuracy of the computation was checked by the conservation of mass and mass flow. The mass source in each control volume was kept as small as

2×10^{-9} percent of the total mass flow, while the total mass-flow imbalance across the cross-stream plane at each station was kept under 2×10^{-7} percent of the total mass flow. Therefore, the total mass flow of the helium and air was virtually unchanged along the entire length of the duct during the computation.

Finite-Element Program

The finite-element program (COMOC), has also been applied to the helium-air mixing experiment. Because of computer storage limitations and long run times when using COMOC, only one-quarter of the duct cross-sectional area was considered. Results for the remaining three quadrants associated with the jet were inferred by symmetry. The additional symmetry boundary condition was approximated by the initial data. There was little change in any of the dependent variables moving transversely between $y = 0$ and $y = -0.00254$ m.

Initial data requirements for COMOC include the three velocity components, temperature, and species mass fraction profiles, and an initial estimate of streamwise pressures. The streamwise velocity component, temperature, and mass fractions were identical with those input into the finite-difference code. Small values of the v and w velocity components on the order of 0.1 percent of the streamwise velocity were assumed, consistent with continuity, to provide a gradient source on the y - and z -momentum equations as no transverse or lateral pressure gradient sources existed. (In the finite-difference program, such sources existed.) No effect was observed on the final downstream results from this assumption. The streamwise pressure gradient was initially assumed to be zero, but as discussed previously, the pressure algorithm rapidly generated a gradient to match computational and actual cross-sectional areas.

Turbulence closure was developed according to mixing-length theory. In this case, the turbulent viscosity μ_t was given by (ref. 2),

$$\mu_t = \rho l_m^2 \left| \frac{\partial u}{\partial z} \right| \quad (20a)$$

where,

$$l_m = C_k (0.01905 - z) D \quad (0 \leq 0.01905 - z \leq \lambda \delta_b / C_k) \quad (20b)$$

$$l_m = \lambda \delta_b D \quad (0.01905 - z > \lambda \delta_b / C_k) \quad (20c)$$

where $C_k = 0.4$, $\lambda = 0.09$, δ_b is the boundary-layer thickness on the wall, and D is the Van Driest damping factor given by

$$D = 1 - \exp \left(\frac{-\tilde{z}}{23.5} \right) \quad (21a)$$

where

$$\tilde{z} = \frac{\tilde{u}(0.01905 - z)}{\nu} \quad (21b)$$

$$\tilde{u} = \sqrt{\frac{\tau_w}{\rho_w}} \quad (21c)$$

and τ_w is the skin friction on the wall, ρ_w the wall density, and ν the kinematic viscosity. The effective Prandtl numbers for enthalpy and mass diffusion were, respectively, 1.0 and 0.4.

Boundary conditions for the three symmetry boundaries were chosen to require that the normal gradient of each of the dependent variables across each of these boundaries vanish. Along the wall boundary, a gradient boundary condition was applied to the streamwise velocity component just off the wall at the outer edge of the sublayer boundary. This condition required that the normal derivative of u be equal at the sublayer boundary to the ratio of the local turbulent shear stress to local turbulent viscosity. Turbulent shear stress was found from a modified relation developed by Patankar and Spalding (ref. 13) through the application of wall functions within the sublayer. Thus, the "gradient boundary condition" simply inverted the basic definition of wall shear and solved for the velocity gradient given shear and viscosity. Although the program can carry the computation directly to the wall, a large number of elements were required to compute the large normal gradients encountered in the sublayer. Since the flow field is conveniently predicted in the sublayer by empirical means, such a computation to the wall was unjustified. The v and w velocity components were required to satisfy a no-slip condition at the wall; that is, they vanish "near" the wall. The normal gradients of both enthalpy and helium mass fraction were required to vanish at the wall, consistent with a no-flux condition there.

The finite-element program also uses a nonuniform grid to discretize the cross-stream (y - z) plane. This plane is spanned by a 6×16 node mesh and 150 triangular finite elements. To march the solution from the initial station ($x = 0.0421$ m) to the final downstream station ($x = 0.7369$ m) required 1326 sec of computer time on the Control Data CYBER 175 computer system with a storage of 265000₈ words.

COMPARISON OF NUMERICAL CALCULATIONS AND EXPERIMENTAL DATA

Downstream computations ($x = 0.7369$ m) from both computer programs are compared with the experimental data in figure 14. Results for streamwise velocity, temperature, and helium mass fraction are plotted from the center plane ($z = 0$) to the duct wall ($z = 0.01905$ m) at five stations along the y -axis. Because the finite-element program calculated only one-quarter of the

center jet region, comparisons for this program are made only at three stations in the positive y-direction (figs. 14(a), 14(b), and 14(c)).

Finite-Difference Program Results

Comparisons of the finite-difference (SHIP) results with experimental data (fig. 14) generally show excellent agreement. The computed streamwise velocity and static temperature give excellent quantitative and qualitative agreement with the experimental data at all five stations along the y-axis. The maximum differences between computational and experimental data are about 6.3 percent for the velocity and 6 percent for the temperature. These maximum differences seem to occur at the measurement points near the duct wall. Several explanations for this discrepancy are possible. The experimentally measured values near the duct wall may be perturbed by the end effects of the duct which may propagate upstream through the subsonic wall boundary layer. Also, data reduction assumed constant total temperature, and this assumption may introduce small errors. On the other hand, in the finite-difference computation, the deficiency near the wall may be due to both the approximate wall boundary condition and the coarse grid spacings selected near the wall. Despite these approximations and uncertainties, the comparisons near the wall are quite satisfactory.

The computed helium mass concentrations are also in good agreement with the experimental data except at the two outermost stations ($y = \pm 0.0127$ m). The disagreements at these stations may be attributed to several sources. First, the downstream measured helium mass flow is experimentally 11 percent higher than the upstream measured helium mass flow; however, the computed helium mass flow is conserved relative to the initial (upstream station) mass-flow data. Second, compared with the experimental data, the mixing of helium with air in the y-direction is relatively slow for the computation; this may be due to an improper estimate of the initial turbulence kinetic energy, dissipation rate, and (three-dimensional) mixing length. In addition, the flow field of the center jet mixing region was assumed to be independent of all other jets in the computation. Practically, there are interactions between two neighboring jet regions, particularly between the central jet and the cross-flow jet. These interactions may have caused nonsymmetric distribution of helium mass concentration at the stations in the positive and negative y-directions. Hence, the helium may be diffused in and out from the boundaries with neighboring regions. Moreover, the absolute values of the helium mass fraction are actually quite small, on the order of less than 0.03. The accuracies of the measurement and the data reduction may limit such a quantitative comparison.

Finite-Element Program Results

Comparisons of the finite-element results with experimental data (figs. 14(a), 14(b), and 14(c)) also show generally good agreement. The static temperatures are in excellent agreement with the experiment, having a maximum difference of only 6.0 percent. The computed streamwise velocities also agree well with the experimental measurements, differing by a maximum of 8.6 percent. Values of the computed helium mass fraction are in good agreement with the

experimental data at the first two lateral stations (figs. 14(a) and 14(b)), but agreement is poor at the outermost station (fig. 14(c)). In addition to the possible sources of disagreement discussed for the finite-difference results, the absence in the finite-element program of a transverse pressure gradient to convect helium away from the jet center line may be the major problem. This deficiency would explain the need of a Prandtl number for mass diffusion (Schmidt number) which is lower than normally observed. Additionally, a coarse element discretization was necessary to maintain reasonable computer time requirements. As a result, the mass flow rates of helium and air were not conserved along the duct, and an overall computational loss in mass flow rate of 15 percent was detected.

Comparison of Program Results

In view of such a complicated three-dimensional flow field, the predictions from both computer programs are considered reasonably good in comparison with the experimental results. Comparisons between the two numerical computations, however, indicate that the finite-difference program provides better overall agreement with experimental data and requires less computer time than the finite-element program.

The superior computational accuracy and run time of the finite-difference program are due primarily to the efficient implicit integrator used to solve the governing equations describing the flow field. This feature allows a very fine nodal discretization of the computational domain, permitting an accurate resolution of gradients within the flow field and requiring reasonable computer run times. The finite-element code currently uses a less efficient explicit predictor-corrector scheme. Recent improvement of the integration algorithm in the finite-element program has, however, resulted in a significant improvement in integration speed and run time. Better integration efficiency also allows the effective use of the two-equation turbulence model by the finite-difference program. The finite-element program is limited by its integrator to an algebraic turbulence model. Finally, the finite-difference program calculates a three-dimensional pressure field, whereas the finite-element program calculates only an axial pressure field. Both transverse pressure gradients are important, however, in mixing flows. Therefore, a three-dimensional pressure algorithm is currently being added to the finite-element program.

Comparison of Computational and Experimental Mixing Efficiencies

In figure 15, the mixing efficiencies calculated along the duct by the two computer programs are presented. The mixing efficiencies at the upstream ($x = 0.0421$ m) and the downstream ($x = 0.7369$ m) measurement stations were also calculated directly from the experimental surveys and are plotted for comparison. Mixing efficiency is a measure of the completeness of mixing between the injectant and the surrounding airstream and is defined at any streamwise station as the fraction of fuel (injectant) that would react if complete reaction occurred without further mixing (ref. 15). To produce a consistent definition in the present calculation of mixing efficiencies, the helium mixed with the airstream was treated as if it were hydrogen, mixed and reacted with the same

airstream. The change in mixing efficiency along the duct is very useful for practical combustor design and helps to determine the combustor size required to achieve desired combustion performance. In experiments, the mixing efficiency can only be obtained at relatively few stations where the flow fields are surveyed. In numerical computations, however, the mixing efficiency can be conveniently calculated at each station along the duct. Such calculations are extremely valuable to supplement the traditional approach based purely on experimentation.

In the comparison of the computational and experimental mixing efficiencies (fig. 15), results again generally agree. However, the computational mixing efficiencies are higher than the experimental value at the initial station ($x = 0.0421$ m). These differences are attributable to both physical and numerical reasons. The experimental mixing efficiency was integrated over the entire region around the central jet by using 819 integration points, while the finite-difference result was integrated over the upper half of the region by using 330 nodes and the finite-element result used 96 nodes (150 finite elements) over one-quarter of the region. Because of strong gradients of helium mass fraction and velocity at the initial station, the use of a different number of integration points naturally results in different calculated mixing efficiencies. Furthermore, the flow field in the central jet region is not exactly symmetric with respect to the symmetry boundaries assumed in the computations; hence, mixing efficiencies calculated in different regions will also be different. At the downstream station ($x = 0.7369$ m), the mixing efficiencies of both computations are in good agreement with the calculation made directly from the experimental survey data.

CONCLUDING REMARKS

Finite-difference and finite-element computer programs have been applied to a three-dimensional nonreacting turbulent mixing experiment. Relative accuracies and efficiencies of the programs have been assessed by comparing their results with the experiment and also by comparing the results of the programs themselves.

In general, both computer programs predict the experimental results and data trends reasonably well. Their predictions were based on the same set of initial experimental data for streamwise velocity, temperature, pressure, and concentration, but the programs used different turbulence models, governing equations, and pressure algorithms. Compared with experimental data at a downstream station, the predictions by the finite-difference program are generally more accurate than those of the finite-element program. Additionally, the finite-difference program is more efficient in both computer storage and computing time than the finite-element program. The superior accuracy of the finite-difference program is due primarily to its efficient integrator, which allows a very fine discretization of the flow field and the application of a more appropriate turbulence closure model. Additionally, the finite-difference program calculates transverse pressure gradients in the duct, whereas the finite-element program is limited to a one-dimensional streamwise pressure field. Both limitations degrade the accuracy of the finite-element program,

and work is currently underway to upgrade both the integrator and the pressure algorithm.

At present, the finite-difference program is preferred for numerical combustor analysis and design. Development of the finite-element program has, however, been underway for significantly less time. Developed to their full potential, both computer programs should provide powerful analysis tools for scramjet engine design.

Langley Research Center
National Aeronautics and Space Administration
Hampton, VA 23665
February 16, 1978

APPENDIX

ASSEMBLED SOLUTION ALGORITHM

In this appendix, the assembled finite-element solution algorithm is developed. To simplify this development, the following notation, which corresponds more closely to that of reference 2, is used:

n_k unit vector normal to k th coordinate direction

x_1 streamwise coordinate x

x_2, x_3 cross-section coordinate corresponding to y and z , respectively

Subscripts:

i coordinate index ranging from 1 to 3

k coordinate index taking on values of 2 and 3

The summation convention is also used.

In this notation, equation (11) becomes

$$\int_{R_m} \{\phi(x_k)\} L(q_m^*) dV - \lambda \oint_{\partial R_m \cap \partial k} \{\phi(x_k)\} l(q_m^*) dS = \{0\} \quad (A1)$$

and equations (7) become

$$\left. \begin{aligned} L(q) &= \kappa \frac{\partial}{\partial x_k} \left[K(q) \frac{\partial q}{\partial x_k} \right] + f\left(q, \frac{\partial q}{\partial x_i}, x_i\right) - g(q, x_1) = 0 \\ l(q) &= a^{(1)} q(x_1, \bar{x}_k) + a^{(2)} K(q) \frac{\partial}{\partial x_k} q(x_1, \bar{x}_k) n_k - a^{(3)} = 0 \end{aligned} \right\} \quad (A2)$$

Now, substituting equations (A2) for L and l into equation (A1) gives

$$\begin{aligned} & \int_{R_m} \{\phi(x_k)\} \kappa \frac{\partial}{\partial x_k} \left[K(q_m^*) \frac{\partial q_m^*}{\partial x_k} \right] dV + \int_{R_m} \{\phi(x_k)\} \left[f\left(q_m^*, \frac{\partial q_m^*}{\partial x_i}, x_i\right) - g(q_m^*, x_1) \right] dV \\ & - \lambda \oint_{\partial R_m \cap \partial R} \{\phi(x_k)\} \left[a_m^{(1)} q_m^*(x_1, \bar{x}_i) + a_m^{(2)} K(q_m^*) \frac{\partial}{\partial x_k} q_m^*(x_1, \bar{x}_i) n_k - a_m^{(3)} \right] dS = \{0\} \end{aligned} \quad (A3)$$

APPENDIX

Equation (A3) presents a potential problem as a consequence of the method of weighted residuals. The differential operators L and ℓ contain derivatives as high as second order with the possibility of introducing discontinuities into the integrands at points in the flow field. The certainty of finite derivatives can be improved if the order of L and ℓ can be reduced.

The Green-Gauss theorem, given by

$$\iiint_V [\Phi \nabla^2 \Psi + (\nabla \Phi) \cdot (\nabla \Psi)] dV = \oint_S (\Phi \nabla \Psi) \cdot dS \quad (A4)$$

provides a means for reducing the order of the operators. The first term of equation (A3) can be modified to fit the form of equation (A4) as follows:

$$\begin{aligned} \int_{R_m} \{\phi\} \kappa \frac{\partial}{\partial x_k} \left[\kappa \frac{\partial q_m^*}{\partial x_k} \right] dV \\ = \kappa \int_{R_m} \frac{\partial}{\partial x_k} \left[\{\phi\} \kappa \frac{\partial q_m^*}{\partial x_k} \right] dV - \kappa \int_{R_m} \frac{\partial \{\phi\}}{\partial x_k} \kappa \frac{\partial q_m^*}{\partial x_k} dV \\ = \kappa \int_{R_m} \left[\{\phi\} \kappa \frac{\partial}{\partial x_k} \frac{\partial q_m^*}{\partial x_k} + \frac{\partial}{\partial x_k} \left(\{\phi\} \kappa \right) \frac{\partial q_m^*}{\partial x_k} \right] dV - \kappa \int_{R_m} \frac{\partial \{\phi\}}{\partial x_k} \kappa \frac{\partial q_m^*}{\partial x_k} dV \end{aligned} \quad (A5)$$

Note that the functional notation has been dropped to simplify the equations. By identifying Φ with $(\{\phi\} \kappa)$ and Ψ with q_m^* , the Green-Gauss theorem can be applied to the first term of equation (A3) to give

$$\int_{R_m} \{\phi\} \kappa \frac{\partial}{\partial x_k} \left[\kappa \frac{\partial q_m^*}{\partial x_k} \right] dV = \kappa \oint_{\partial R_m} \{\phi\} \kappa \frac{\partial q_m^*}{\partial x_k} n_k dS - \kappa \int_{R_m} \frac{\partial \{\phi\}}{\partial x_k} \kappa \frac{\partial q_m^*}{\partial x_k} dV \quad (A6)$$

APPENDIX

Substituting equation (A6) into equation (A3) then gives

$$\begin{aligned} & \kappa \int_{\partial R_m} \{\phi\} K \frac{\partial q_m^*}{\partial x_k} n_k dS - \kappa \int_{R_m} \frac{\partial \{\phi\}}{\partial x_k} K \frac{\partial q_m^*}{\partial x_k} dV + \int_{R_m} \{\phi\} [f_m^* - g_m^*] dV \\ & - \lambda \oint_{\partial R_m \cap \partial R} \{\phi\} \left[a_m^{(1)} q_m^* + a_m^{(2)} K \frac{\partial q_m^*}{\partial x_k} n_k - a_m^{(3)} \right] dS = \{0\} \end{aligned} \quad (A7)$$

where $f_m^* = f(q_m^*, \partial q_m^* / \partial x_i, x_i)$ and $g_m^* = g(q_m^*, x_1)$. Note that the derivative order of equation (A7) has been lowered by 1 with respect to equation (A3).

Now, since λ is an arbitrary algebraic multiplier, choose $\lambda a_m^{(2)}$ equal to κ for $\partial R_m \cap \partial R$ nonvanishing (ref. 7); this choice causes the first term of equation (A7) to cancel with the second term of the fourth integral only where ∂R_m and ∂R correspond. This leaves

$$\begin{aligned} & \kappa \oint_{\substack{\partial R_m \\ \partial R_m \cap \partial R = 0}} \{\phi\} K \frac{\partial q_m^*}{\partial x_k} n_k dS - \kappa \int_{R_m} \frac{\partial \{\phi\}}{\partial x_k} K \frac{\partial q_m^*}{\partial x_k} dV + \int_{R_m} \{\phi\} [f_m^* - g_m^*] dV \\ & - \kappa \oint_{\partial R_m \cap \partial R} \{\phi\} \left[a_m^{(1)'} q_m^* - a_m^{(3)'} \right] dS = \{0\} \end{aligned} \quad (A8)$$

where $a_m^{(1)'} = a_m^{(1)} / a_m^{(2)}$ and $a_m^{(3)'} = a_m^{(3)} / a_m^{(2)}$.

Equation (A8) provides the solution algorithm for each finite-element subdomain. To establish the solution for the entire duct cross-sectional plane (the global solution), equation (A8) is first evaluated for each of the M finite elements ($m = 1, 2, \dots, M$). For each element, three first-order ordinary differential equations result for each dependent variable. These three equations are now summed (assembled) over the M finite elements according to Boolean algebra (symbol \cup) to give a $3 \times M$ equation system that will produce the global solution. Thus, the global solution is

APPENDIX

$$\cup \left[\kappa \oint_{\substack{\partial R_m \\ \partial R_m \cap \partial R = 0}} \{\phi\} \kappa \frac{\partial q_m^*}{\partial x_k} n_k dS - \kappa \int_{R_m} \frac{\partial \{\phi\}}{\partial x_k} \kappa \frac{\partial q_m^*}{\partial x_k} dV + \int_{R_m} \{\phi\} (f_m^* - g_m^*) dV \right. \\ \left. - \kappa \oint_{\partial R_m \cap \partial R} \{\phi\} (a_m^{(1)'} q_m^* - a_m^{(3)'}) dS \right] = \{0\} \quad (A9)$$

Now, in accordance with reference 14, since $\{\phi\}$ is a linear function, the surface contributions resulting from the first integral of equation (A9) can be made to cancel in pairs upon assembly. This result is physically meaningful since the evaluation of the surface integral with outward pointing normal about a common side of adjacent element pairs would give equal and opposite values that would cancel when their algebraic sum was taken. Then, equation (A9) becomes

$$\cup \left[-\kappa \int_{R_m} \frac{\partial \{\phi\}}{\partial x_k} \kappa \frac{\partial q_m^*}{\partial x_k} dV + \int_{R_m} \{\phi\} (f_m^* - g_m^*) dV \right. \\ \left. - \kappa \oint_{\partial R_m \cap \partial R} \{\phi\} (a_m^{(1)'} q_m^* - a_m^{(3)'}) dS \right] = \{0\} \quad (A10)$$

After the notation is changed to that of the main text, equation (A10) is identical to equation (12) and is the basis of the solution algorithm for all dependent variables in COMOC.

REFERENCES

1. Markatos, N. C.; Spalding, D. B.; and Tatchell, D. G.: Combustion of Hydrogen Injected Into a Supersonic Airstream (The SHIP Computer Program). NASA CR-2802, 1977.
2. Zelazney, S. W.; Baker, A. J.; and Rushmore, W. L.: Modeling of Three-Dimensional Mixing and Reacting Ducted Flows. NASA CR-2661, 1976.
3. Patankar, S. V.; and Spalding, D. B.: A Calculation Procedure for Heat, Mass and Momentum Transfer in Three-Dimensional Parabolic Flows. Int. J. Heat & Mass Transfer, vol. 15, no. 10, Oct. 1972, pp. 1787-1806.
4. Baker, A. J.: Finite Element Solution Theory for Three-Dimensional Boundary Flows. Comput. Methods Appl. Mech. & Eng., vol. 4, no. 3, Nov. 1974, pp. 367-386.
5. Curr, R. M.; Sharma, Devraj; and Tatchell, D. G.: Numerical Predictions of Some Three-Dimensional Boundary Layers in Ducts. Comput. Methods Appl. Mech. & Eng., vol. 1, no. 2, Aug. 1972, pp. 143-158.
6. Patankar, S. V.; Pratap, V. S.; and Spalding, D. B.: Prediction of Turbulent Flow in Curved Pipes. J. Fluid Mech., vol. 67, pt. 3, Feb. 11, 1975, pp. 583-595.
7. Baker, A. J.; and Zelazny, S. W.: COMOC: Three-Dimensional Boundary Region Variant. Theoretical Manual and User's Guide. NASA CR-132450, 1974.
8. Baker, A. J.; and Zelazny, S. W.: A Theoretical Study of Mixing Downstream of Transverse Injection Into a Supersonic Boundary Layer. NASA CR-112254, 1972.
9. Rogers, R. Clayton: Mixing of Hydrogen Injected From Multiple Injectors Normal to a Supersonic Airstream. NASA TN D-6474, 1971.
10. Dyer, D. F.; Maples, G.; and Spalding, D. B.: Combustion of Hydrogen Injected Into a Supersonic Airstream (A Guide to the HISS Computer Program). NASA CR-2655, 1976.
11. Pan, Y. S.: Evaluation of the Three-Dimensional Parabolic Flow Computer Program SHIP. NASA TM-74094, 1978.
12. Spalding, D. B.: A Novel Finite Difference Formulation for Differential Expressions Involving Both First and Second Derivatives. Int. J. Numerical Methods Eng., vol. 4, July-Aug. 1972, pp. 551-559.
13. Patankar, S. V.; and Spalding, D. B.: Heat and Mass Transfer in Boundary Layers. Second ed. Int. Textbook Co. Ltd. (London), c.1970.
14. Baker, A. J.: A Finite Element Solution Algorithm for the Navier-Stokes Equations. NASA CR-2391, 1974.

15. McClinton, Charles R.: Evaluation of Scramjet Combustor Performance Using Cold Nonreactive Mixing Tests. AIAA Paper No. 76-47, Jan. 1976.
16. Pinckney, S. Z.: A Short Static-Pressure Probe Design for Supersonic Flow. NASA TN D-7978, 1975.
17. Launder, B. E.; Morse, A.; Rodi, W.; and Spalding, D. B.: Prediction of Free Shear Flows - A Comparison of the Performance of Six Turbulence Models. Free Turbulent Shear Flows. Volume I - Conference Proceedings, NASA SP-321, 1973, pp. 361-426.

TABLE I.- TEST CONDITIONS

Streamwise station, m	$P_{T,A}$, MPa	$P_{T,I}$, MPa	$T_{T,A}$, K	$T_{T,I}$, K	\dot{m}_A , kg/sec	\dot{m}_I , kg/sec
x = 0.0421	1.655	3.266	294	294	5.960	0.1425
x = 0.7369	1.600	3.791	294	294	5.826	0.1582

TABLE II.- EXPERIMENTAL DATA AT UPSTREAM STATION ($x = 0.0421$ m)

y, m	z, m	u, m/sec	p, MPa	T, K	f _{He} , percent
-0.0127	0.0173	436	0.1172	201	0
	.0127	497	.1145	171	.0484
	.0064	427	.1124	203	.0971
	0	460	.1131	189	0
	-.0058	457	.1124	191	0
	-.0119	451	.1145	193	.0318
	-.0160	280	.1172	256	0
-0.0102	0.0173	424	0.1172	206	0
	.0127	500	.1145	171	0
	.0064	433	.1124	202	.0762
	0	485	.1131	182	.873
	-.0058	460	.1124	189	.00138
	-.0119	451	.1145	192	0
	-.0160	295	.1172	251	0
-0.0076	0.0173	427	0.1172	204	0
	.0127	494	.1151	174	0
	.0064	436	.1124	201	.0804
	0	512	.1124	186	4.67
	-.0058	457	.1124	191	.0443
	-.0119	451	.1151	193	0
	-.0160	311	.1172	246	0
-0.0051	0.0173	457	0.1172	191	0
	.0127	494	.1151	173	0
	.0064	436	.1124	203	.972
	0	750	.1124	163	26.7
	-.0058	454	.1124	192	.0166
	-.0119	451	.1151	193	.00138
	-.0160	305	.1172	248	0
-0.0025	0.0173	469	0.1172	185	0
	.0127	494	.1151	174	.289
	.0064	472	.1124	204	5.27
	0	1152	.1117	143	80.2
	-.0058	451	.1124	195	.337
	-.0119	445	.1151	196	0
	-.0160	348	.1172	234	0

TABLE II.- Concluded

y, m	z, m	u, m/sec	p, MPa	T, K	f _{He} , percent
0	0.0173	469	0.1165	184	0
	.0127	491	.1145	175	0
	.0064	518	.1124	199	9.69
	0	1140	.1103	143	77.7
	-.0058	451	.1124	195	.367
	-.0119	445	.1145	196	0
	-.0160	314	.1165	246	0
0.0025	0.0173	463	0.1151	188	0
	.0127	500	.1131	170	0
	.0064	445	.1117	199	.760
	0	686	.1089	170	20.9
	-.0058	457	.1117	190	.0429
	-.0119	454	.1131	192	0
	-.0160	320	.1151	244	0
0.0051	0.0173	454	0.1103	192	0
	.0127	503	.1117	169	0
	.0064	439	.1110	199	.0762
	0	500	.1069	179	1.80
	-.0058	460	.1110	189	.00276
	-.0119	457	.1117	191	0
	-.0160	323	.1103	243	0
0.0076	0.1173	433	0.1089	201	0
	.0127	506	.1117	168	0
	.0064	439	.1103	199	.0734
	0	482	.1055	179	.214
	-.0058	466	.1103	186	.00276
	-.0119	460	.1117	189	0
	-.0160	344	.1089	236	0

TABLE III.- EXPERIMENTAL DATA AT DOWNSTREAM STATION ($x = 0.7369$ m)

y, m	z, m	u, m/sec	p, MPa	T, K	f _{He} , percent
-0.0127	0.0173	338	0.1793	242	2.00
	.0127	400	.1703	226	2.34
	.0064	436	.1648	210	2.84
	0	445	.1669	207	3.02
	-.0058	438	.1600	208	2.47
	-.0119	392	.1613	223	1.59
	-.0160	324	.1641	244	1.00
-0.0063	0.0173	347	0.1786	238	1.76
	.0127	403	.1724	221	2.29
	.0064	438	.1669	210	3.09
	0	450	.1669	206	3.33
	-.0058	440	.1613	208	2.75
	-.0119	395	.1610	222	1.76
	-.0160	330	.1627	243	1.10
0	0.0173	342	0.1779	240	1.59
	.0127	399	.1710	222	2.11
	.0064	435	.1655	211	2.96
	0	452	.1620	205	3.29
	-.0058	448	.1565	205	2.82
	-.0119	407	.1586	218	1.85
	-.0160	431	.1620	239	1.06
0.0063	0.0173	370	0.1544	229	1.21
	.0127	410	.1620	217	1.79
	.0064	436	.1600	209	2.56
	0	456	.1496	202	2.90
	-.0058	455	.1469	202	2.54
	-.0119	425	.1503	211	1.78
	-.0160	361	.1524	232	.95
0.0127	0.0173	360	0.1627	233	1.03
	.0127	407	.1641	217	1.61
	.0064	435	.1606	209	2.43
	0	453	.1503	203	2.84
	-.0058	454	.1475	202	2.63
	-.0119	420	.1523	213	1.92
	-.0160	359	.1538	233	1.11

TABLE IV.- COMPARISON OF THE TWO COMPUTATIONS BASED ON SHIP AND COMOC

	SHIP	COMOC
Governing equations	Parabolic type of Navier-Stokes equations	Parabolic type of Navier-Stokes equations with additional boundary-layer-type simplifications
Pressure gradient	Streamwise and transverse	Streamwise only
Turbulence model	"k- ϵ " two-equation model	Mixing-length model
Reaction model	Equilibrium reactions	Complete reaction
Numerical scheme	Finite difference	Finite element
Region of computation (fig. 12)	ABCDEFA	ABCFA
Number of grid points	11 \times 30	6 \times 16
Input initial flow field data	u, p, T, f_{He} (v = w = 0)	u, p, T, f^{α} (v, w estimated from continuity equation)
Number of streamwise stations computed	690 steps	351 steps
Total computer storage	77400g	265000g
Computing time on Control Data CYBER 175	261 sec	1326 sec

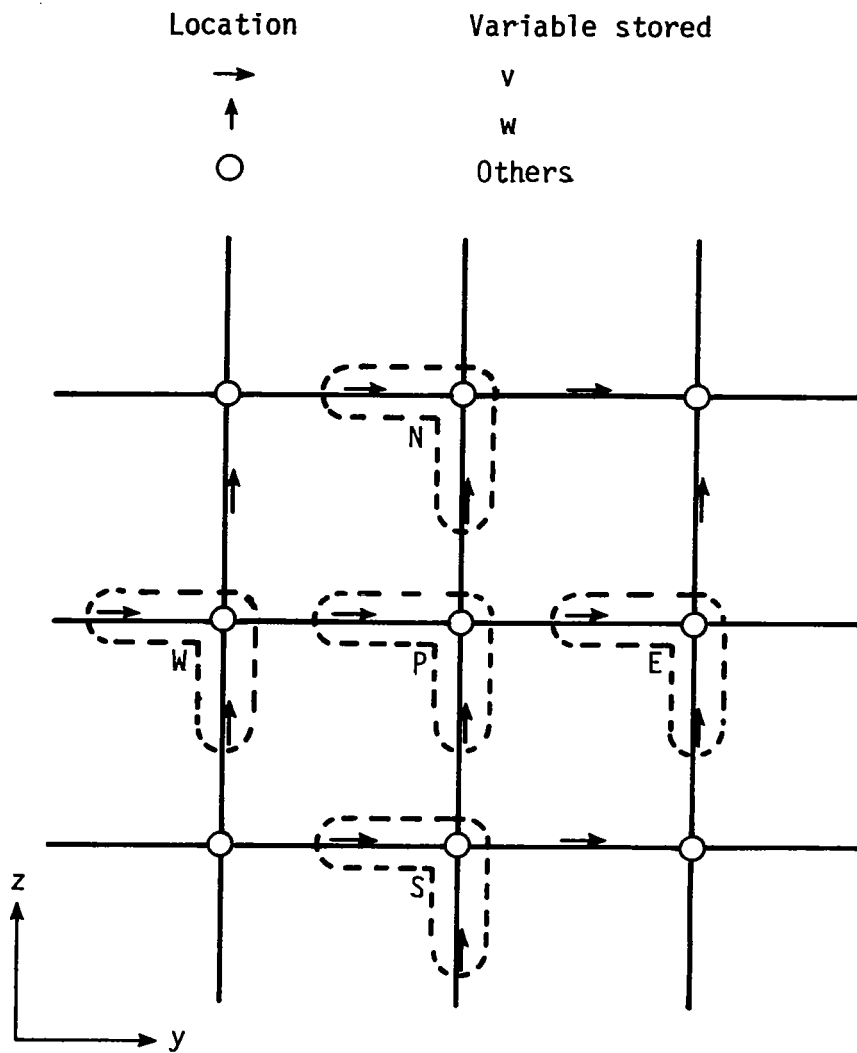


Figure 1.- Staggered grid system used in finite-difference program.

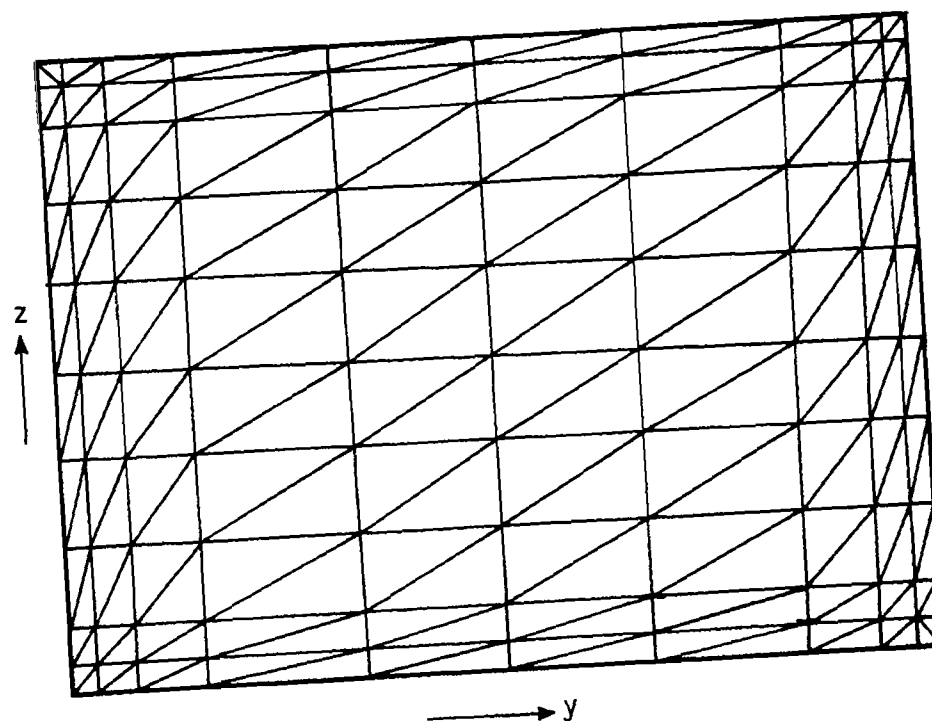


Figure 2.- Triangular finite-element discretization used in finite-element program.

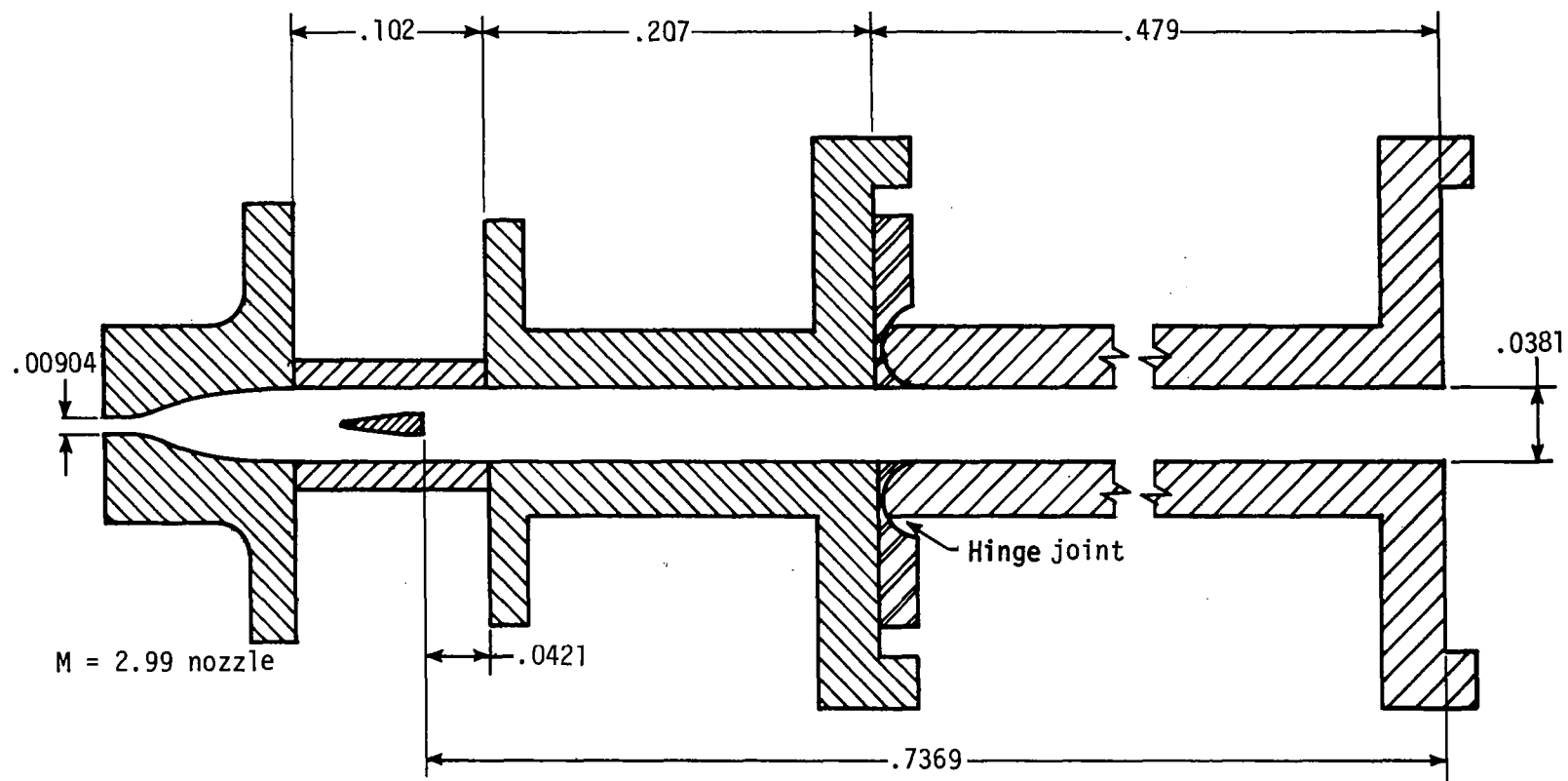


Figure 3.- Injector strut and combustor duct. All dimensions are in meters.

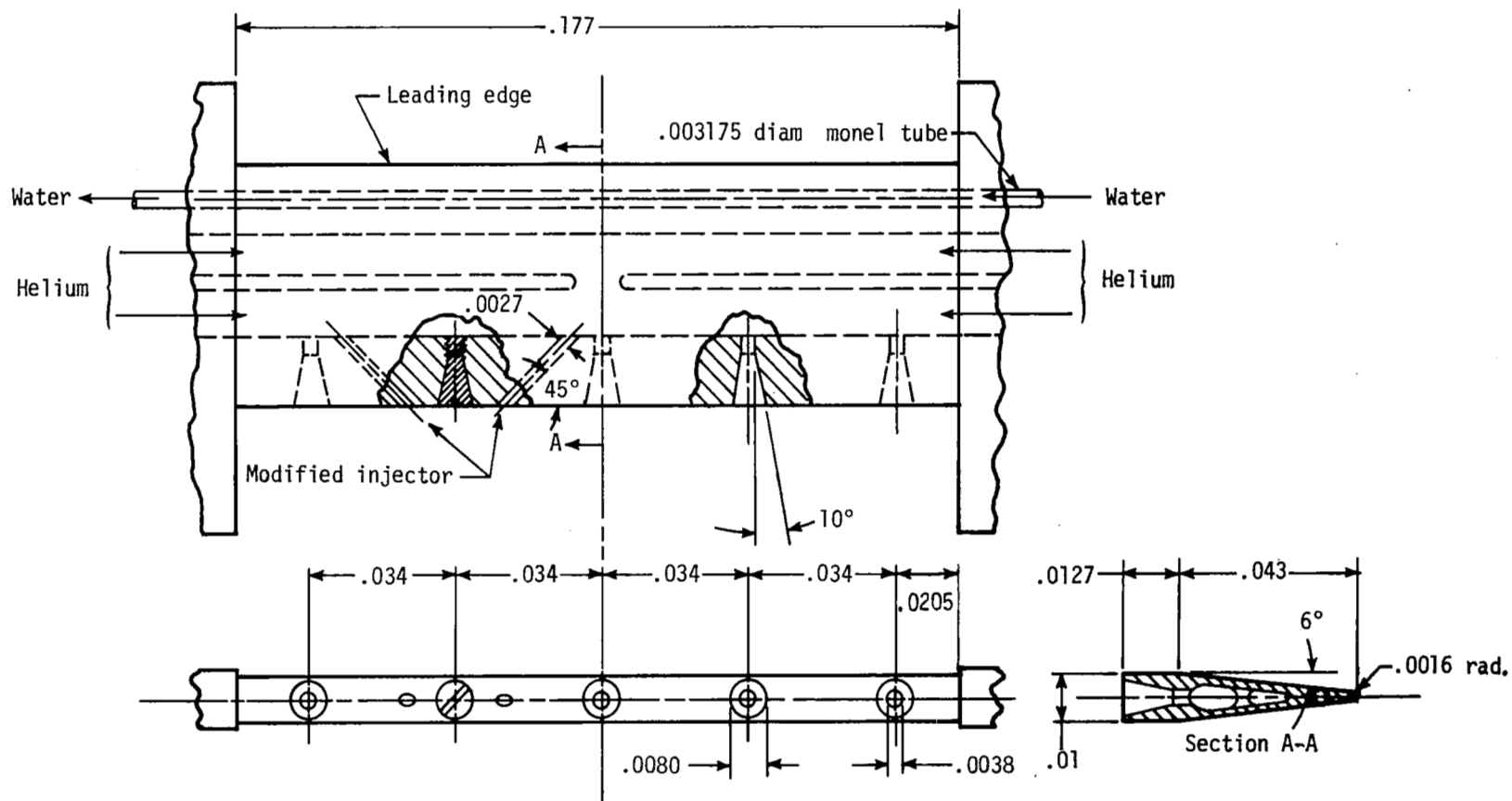
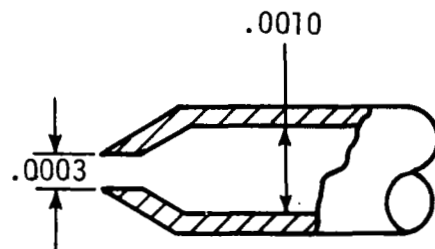
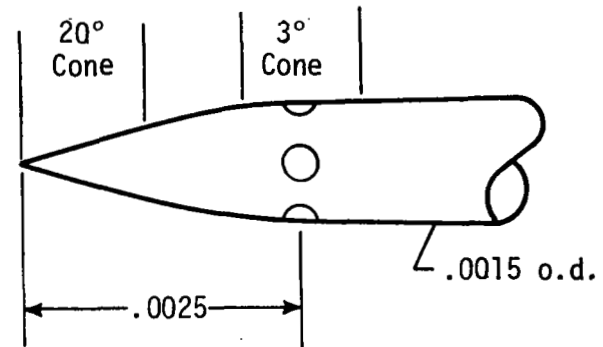


Figure 4.- Strut injectors. All dimensions are in meters.



(a) Pitot probe.



(b) Static probe.

Figure 5.- Probe tip details. All dimensions are in meters.

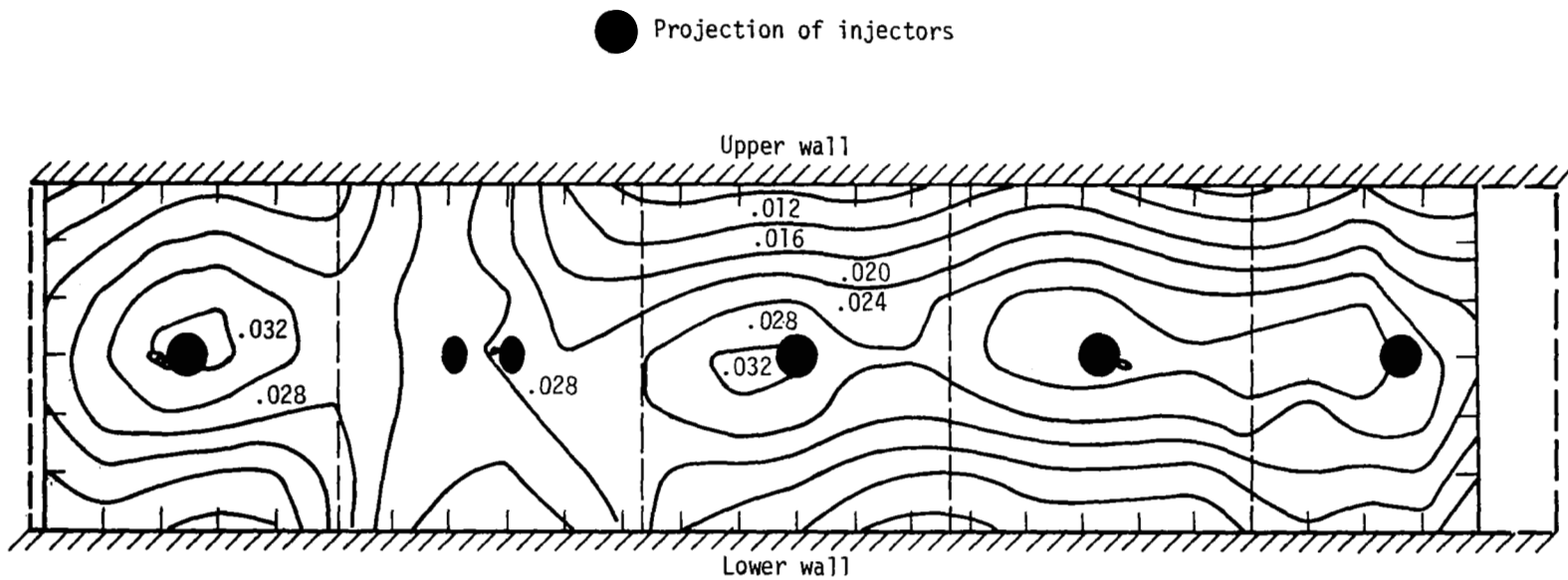


Figure 6.- Helium mass fraction contours of duct cross section at $x = 0.7369$ m.

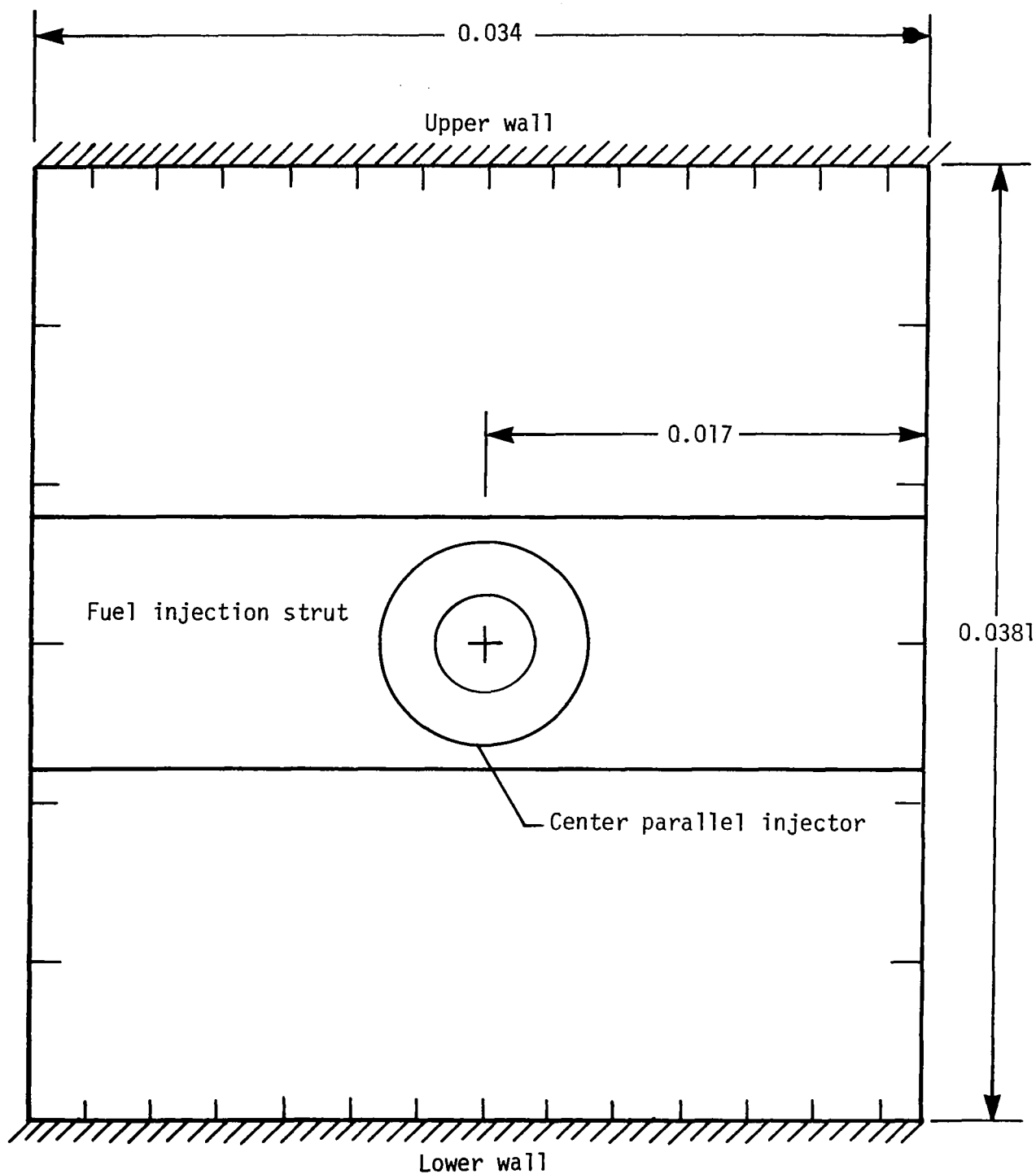
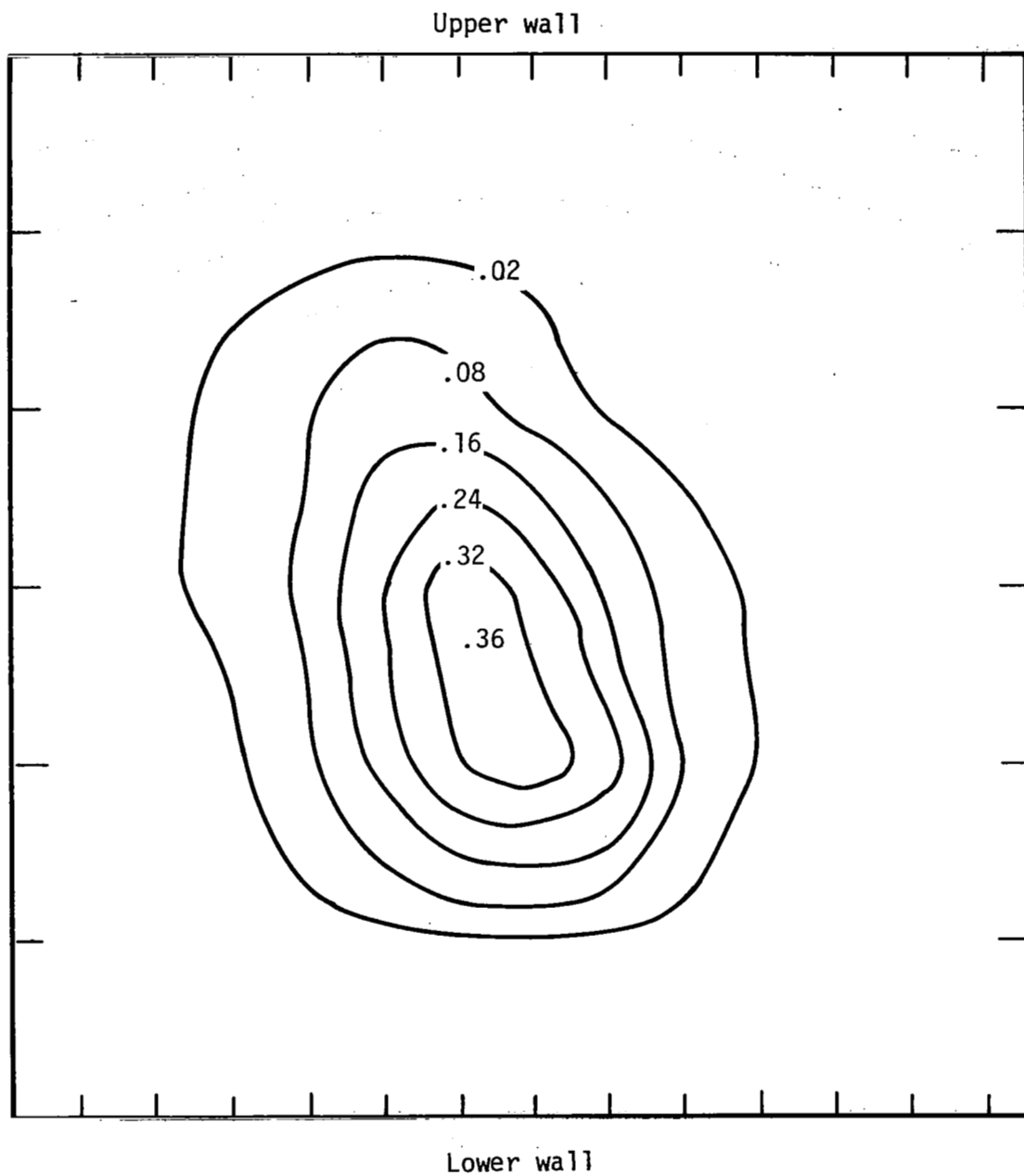
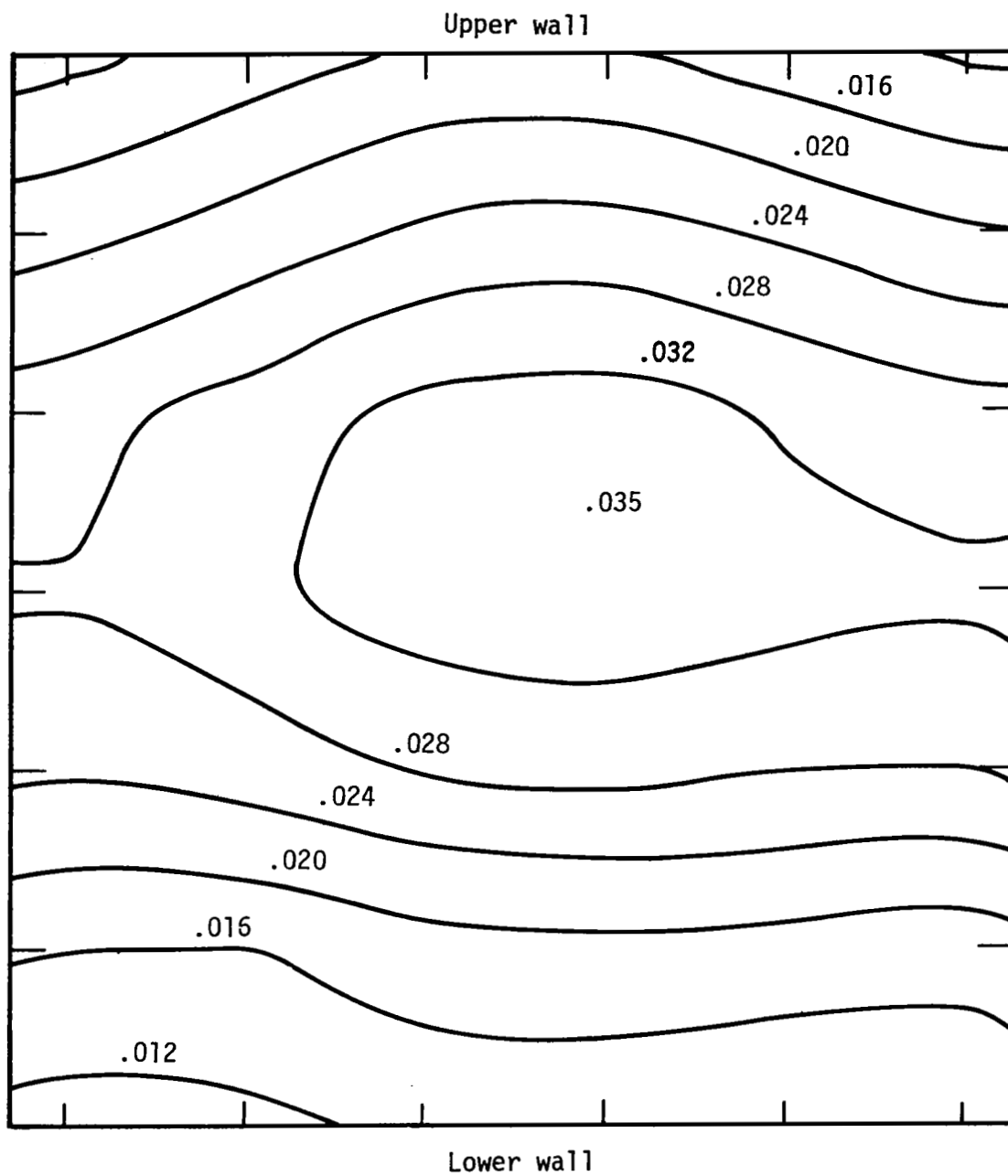


Figure 7.- Mixing region of center jet. Tick marks represent horizontal and vertical location of probe during survey. Dimensions are in meters.



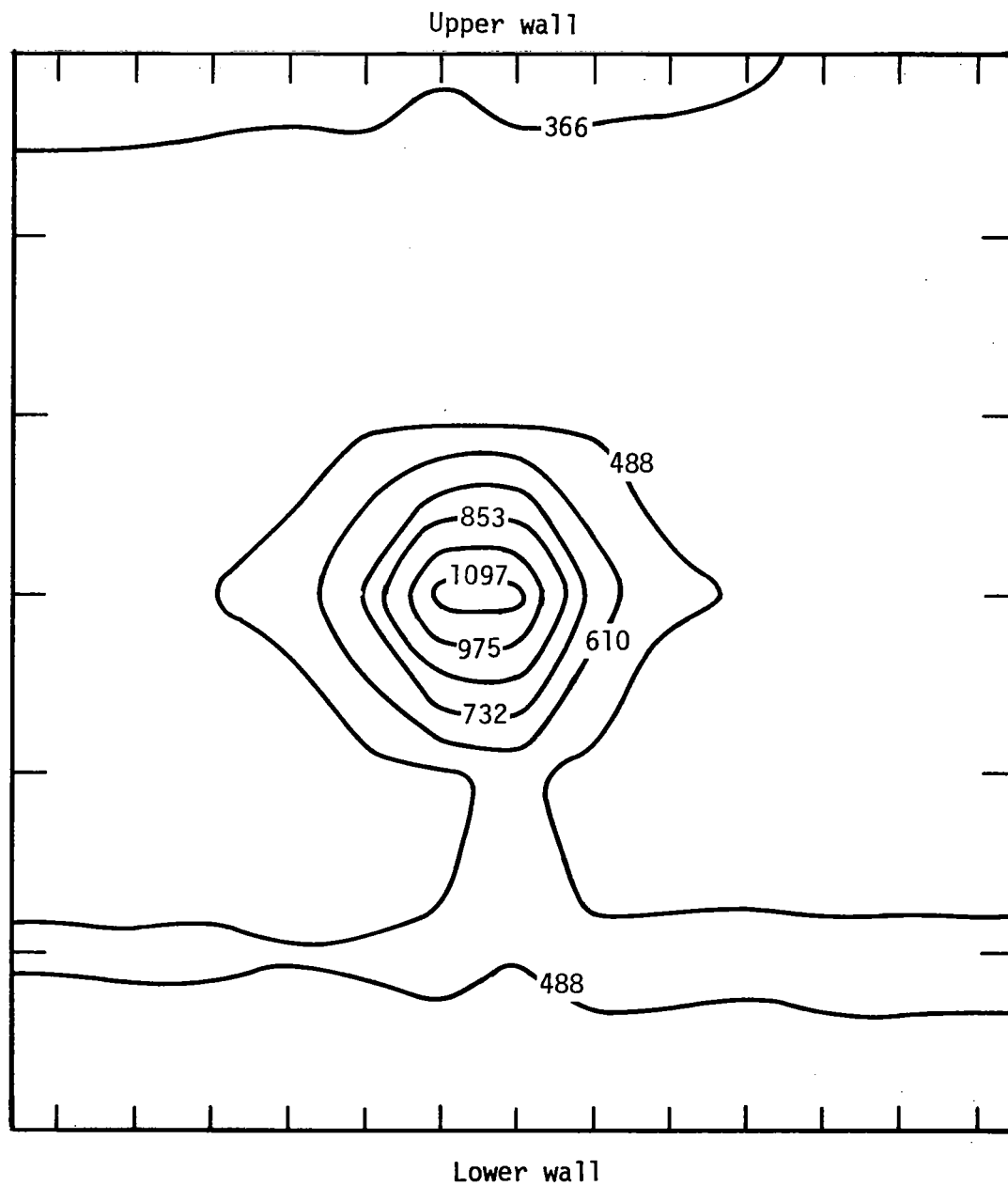
(a) $x = 0.0421$ m. $\dot{m}_{\text{He}} = 0.8433$.

Figure 8.- Helium mass fraction contours of center jet mixing region.



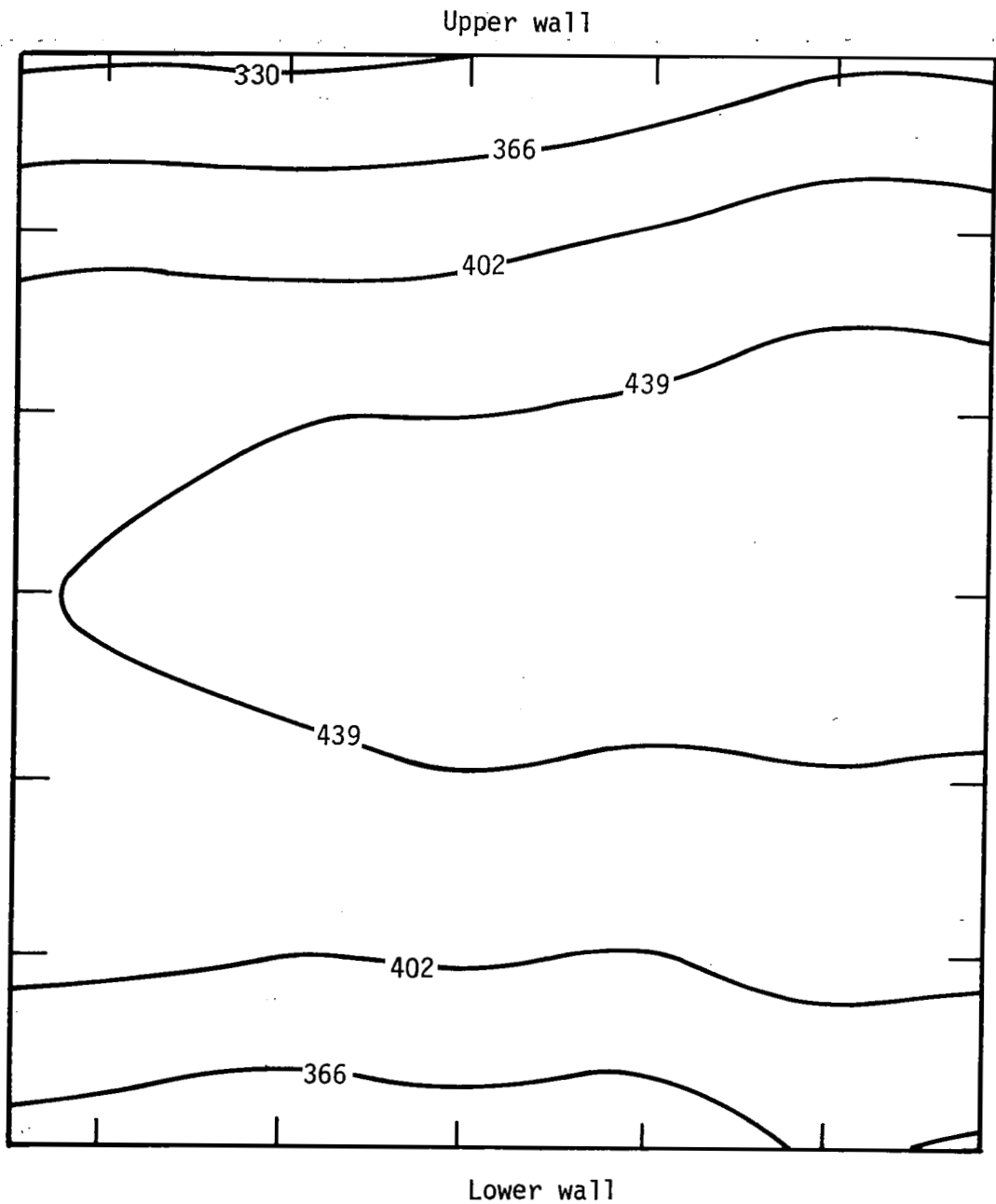
(b) $x = 0.7369 \text{ m}$. $\dot{m}_{\text{He}} \approx 0.9015$.

Figure 8.- Concluded.



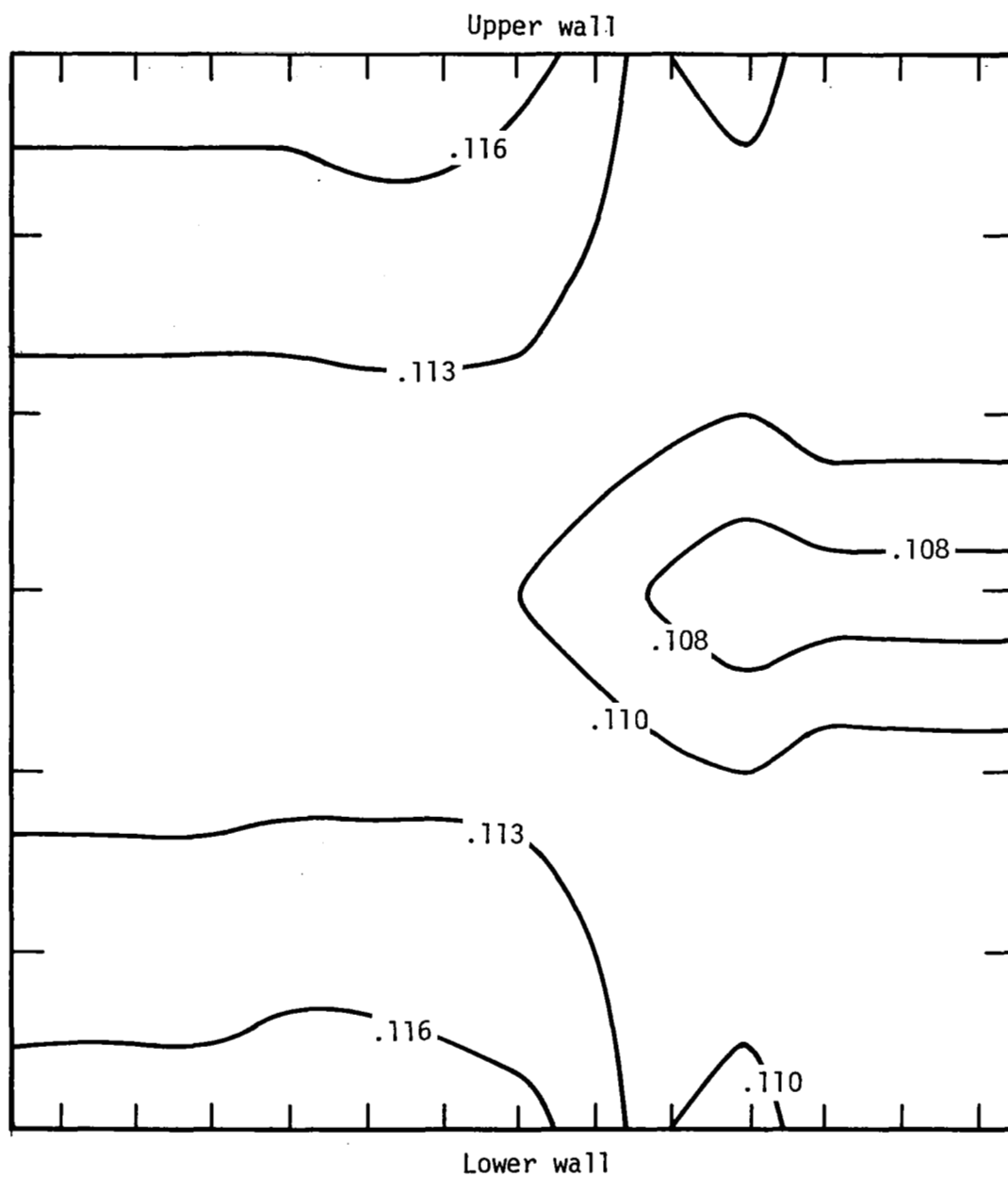
(a) $x = 0.0421$ m.

Figure 9.- Streamwise velocity contours of center jet mixing region.
Velocity is given in m/sec.



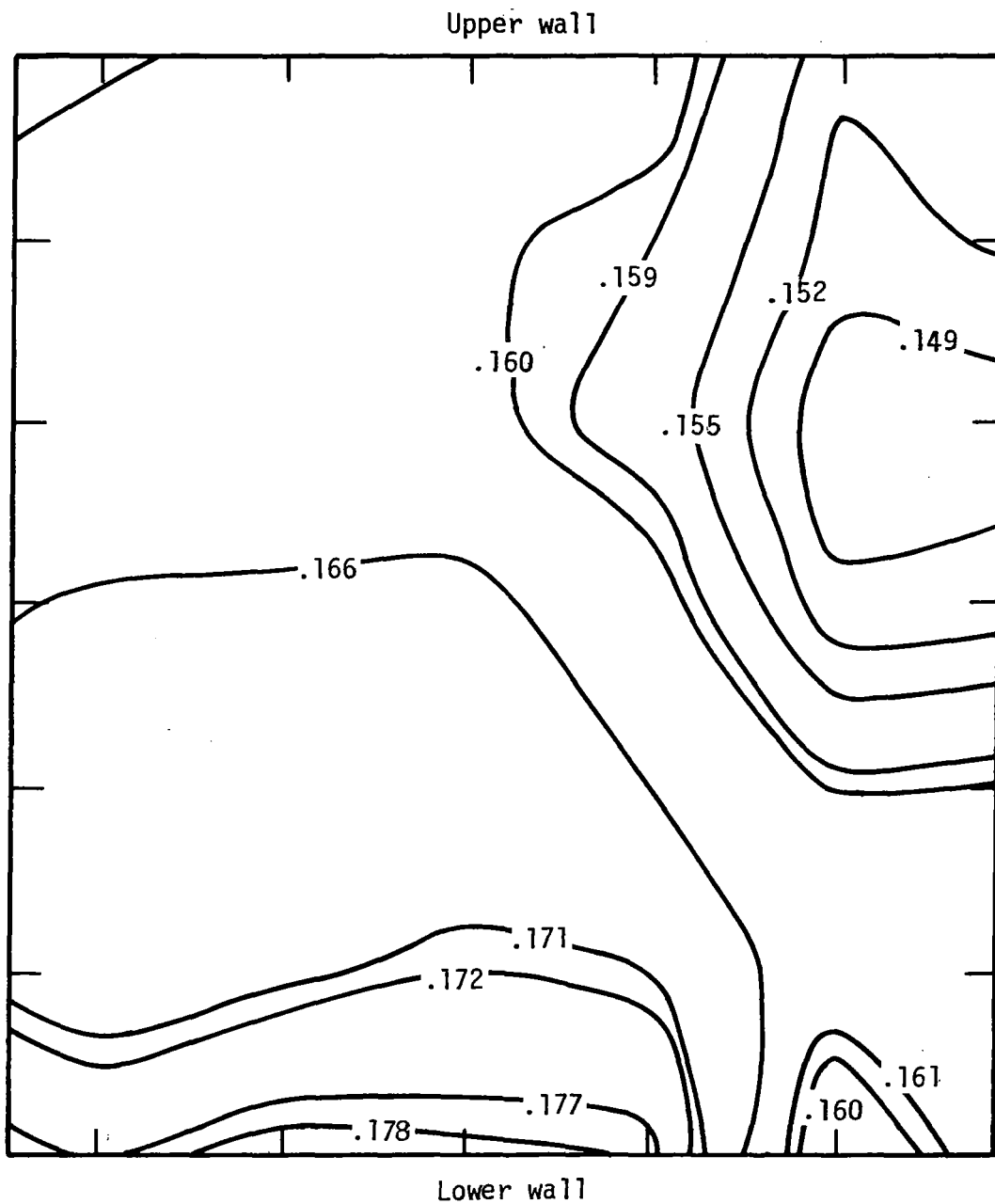
(b) $x \approx 0.7369$ m.

Figure 9.- Concluded.



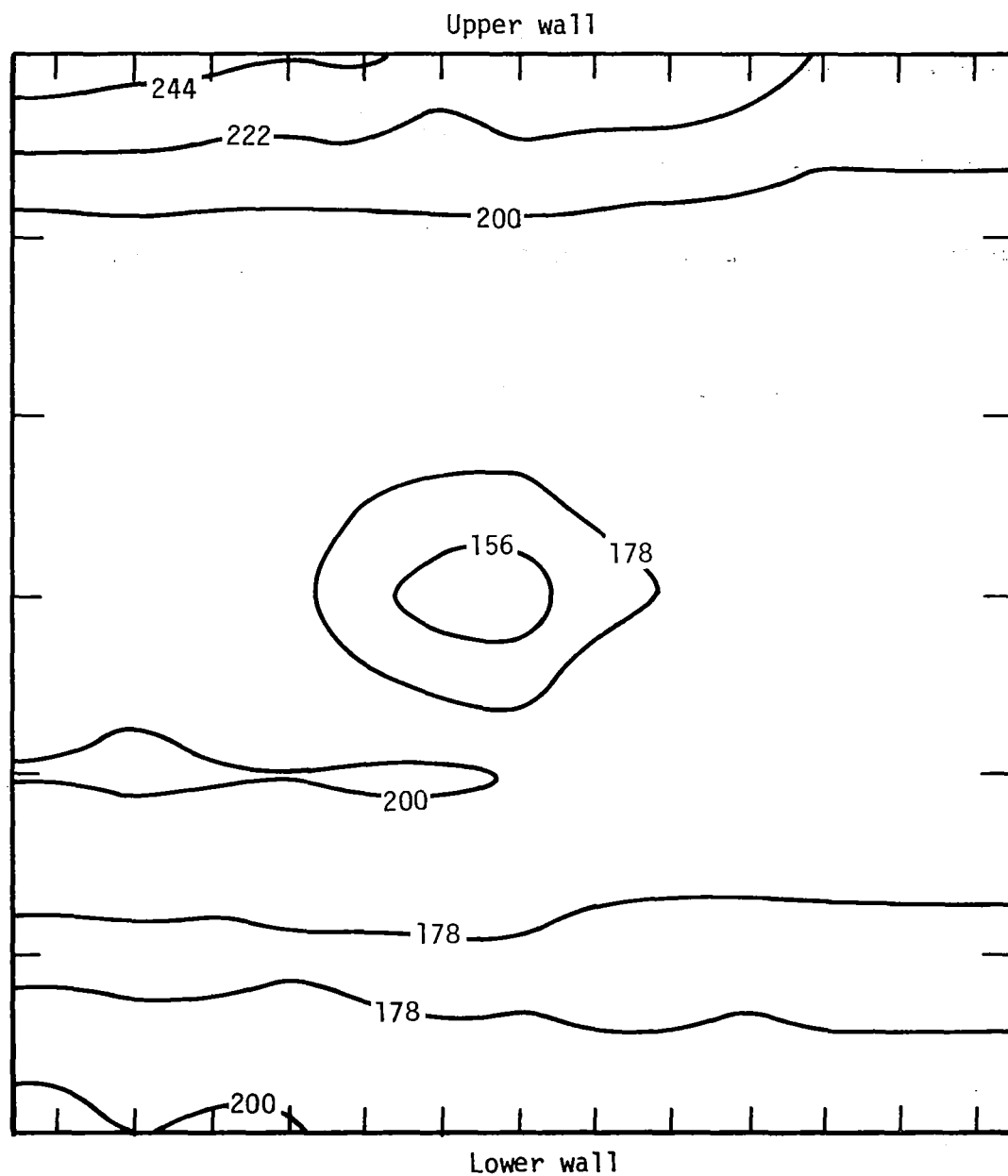
(a) $x = 0.0421$ m.

Figure 10.- Static pressure contours of center jet mixing region.
Static pressure is given in mPa.



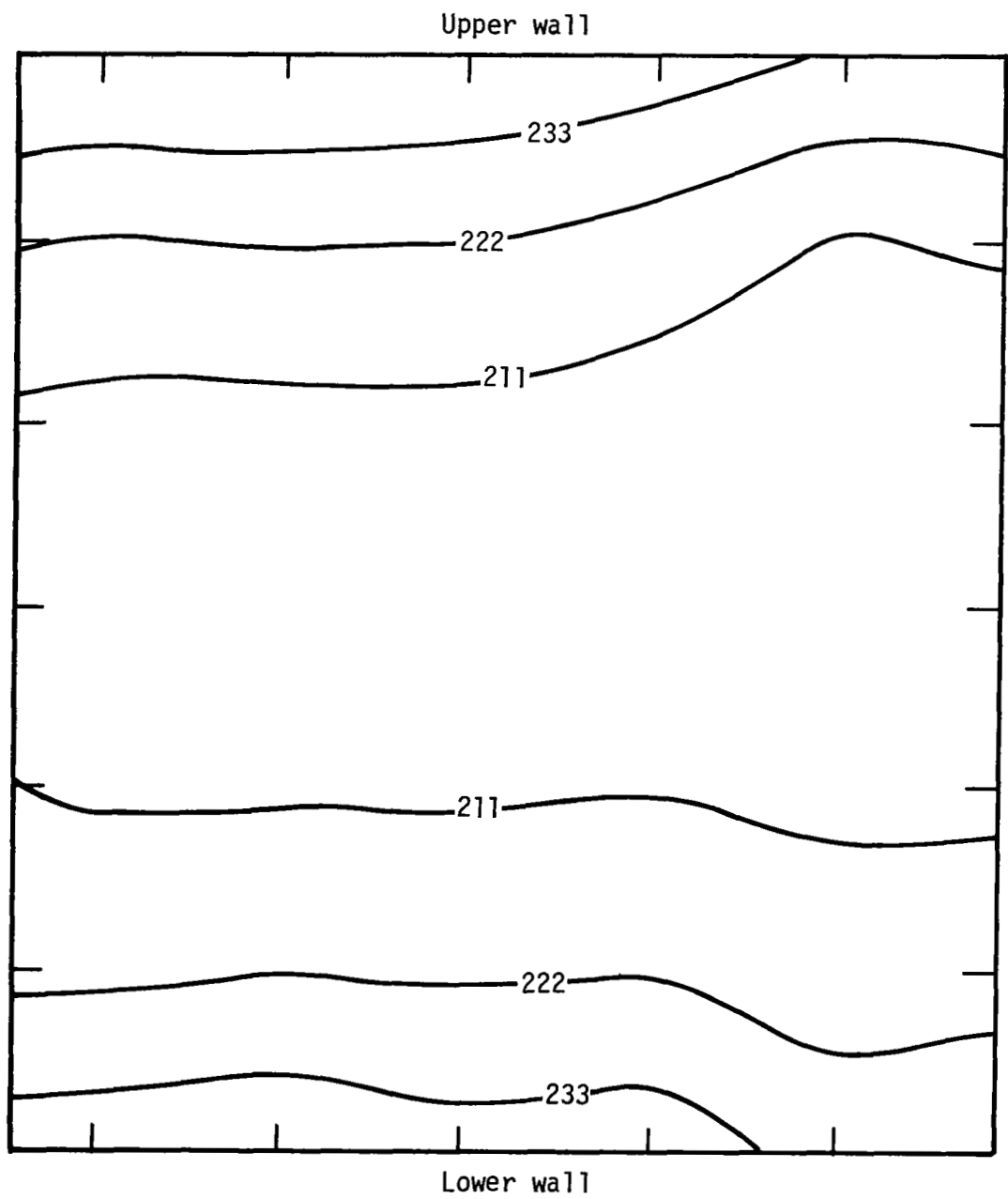
(b) $x = 0.7369$ m.

Figure 10.- Concluded.



(a) $x = 0.0421$ m.

Figure 11.- Static temperature contours of center jet mixing region.
Static temperature is given in K.



(b) $x \approx 0.7369$ m.

Figure 11.- Concluded.

ABCDEFA Finite-difference domain

ABCFA Finite-element domain

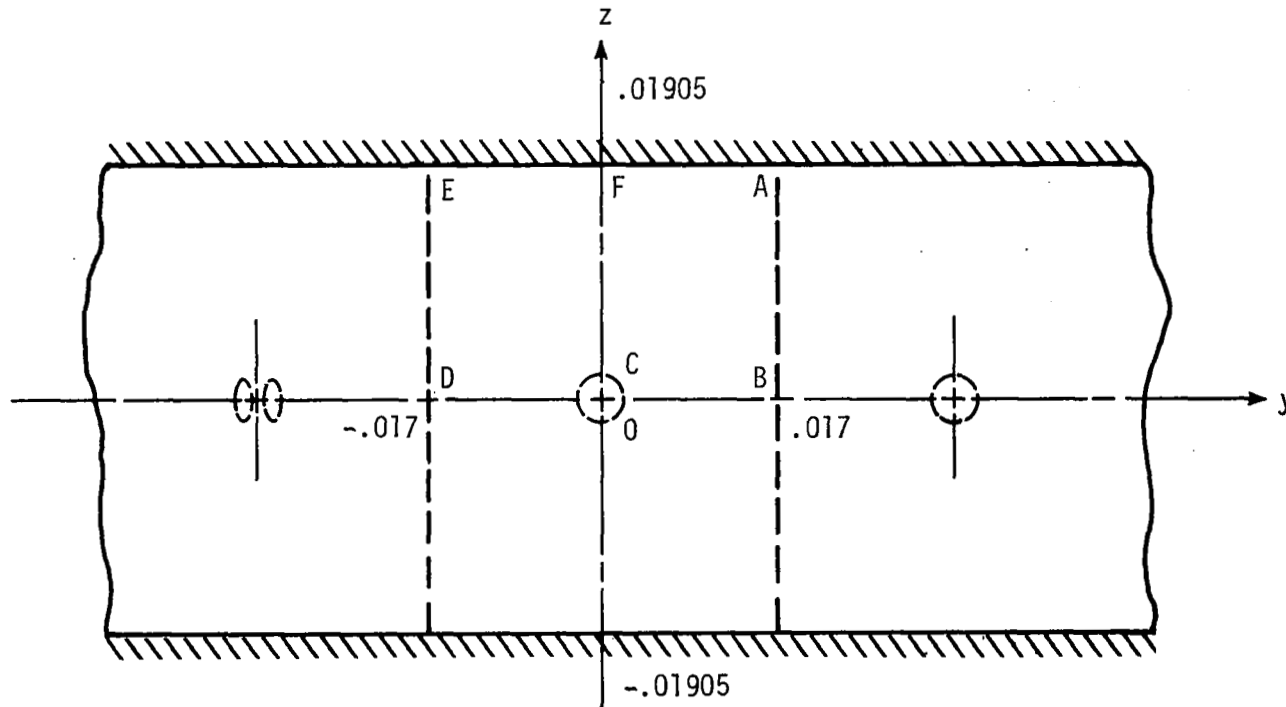
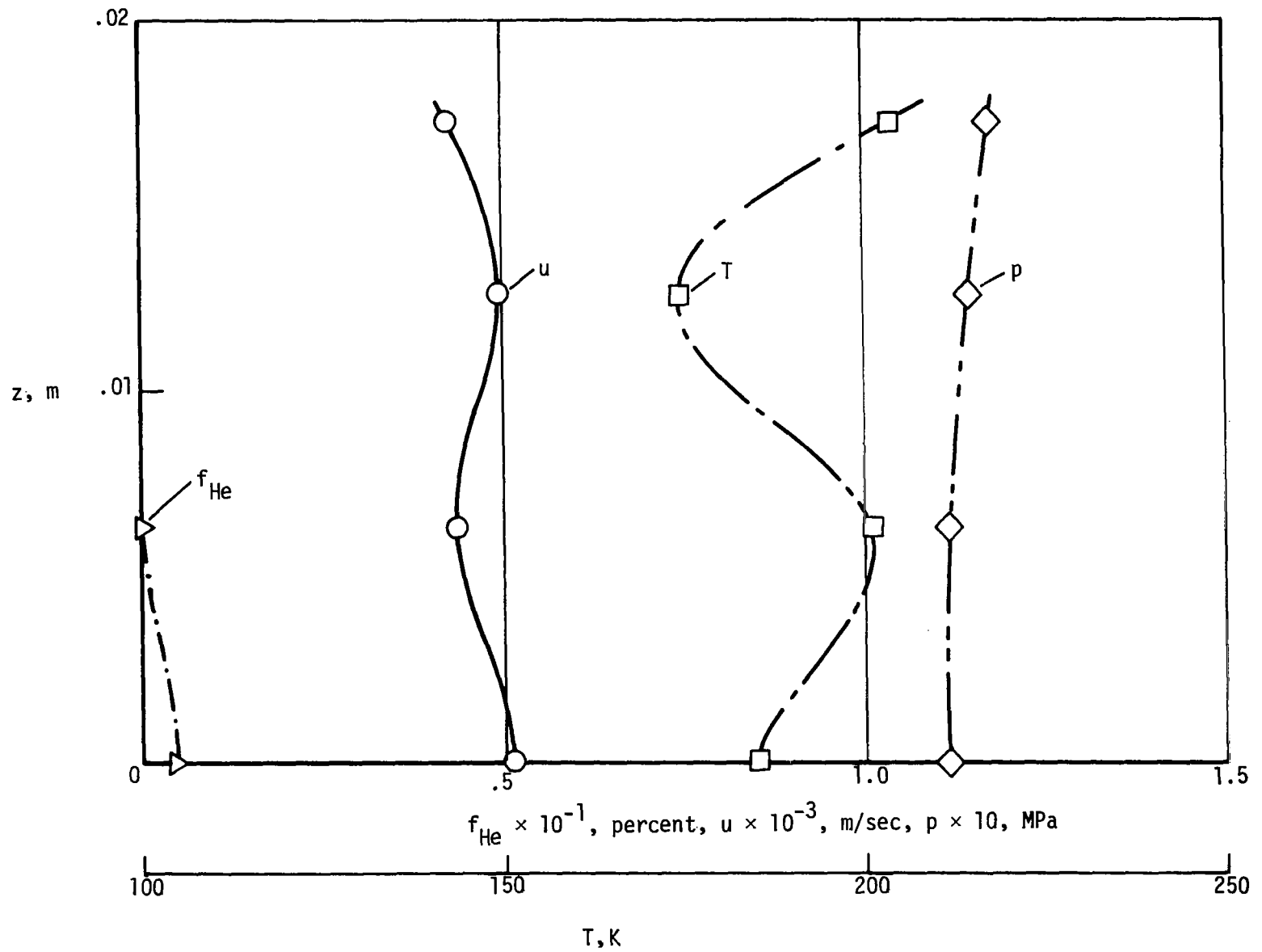
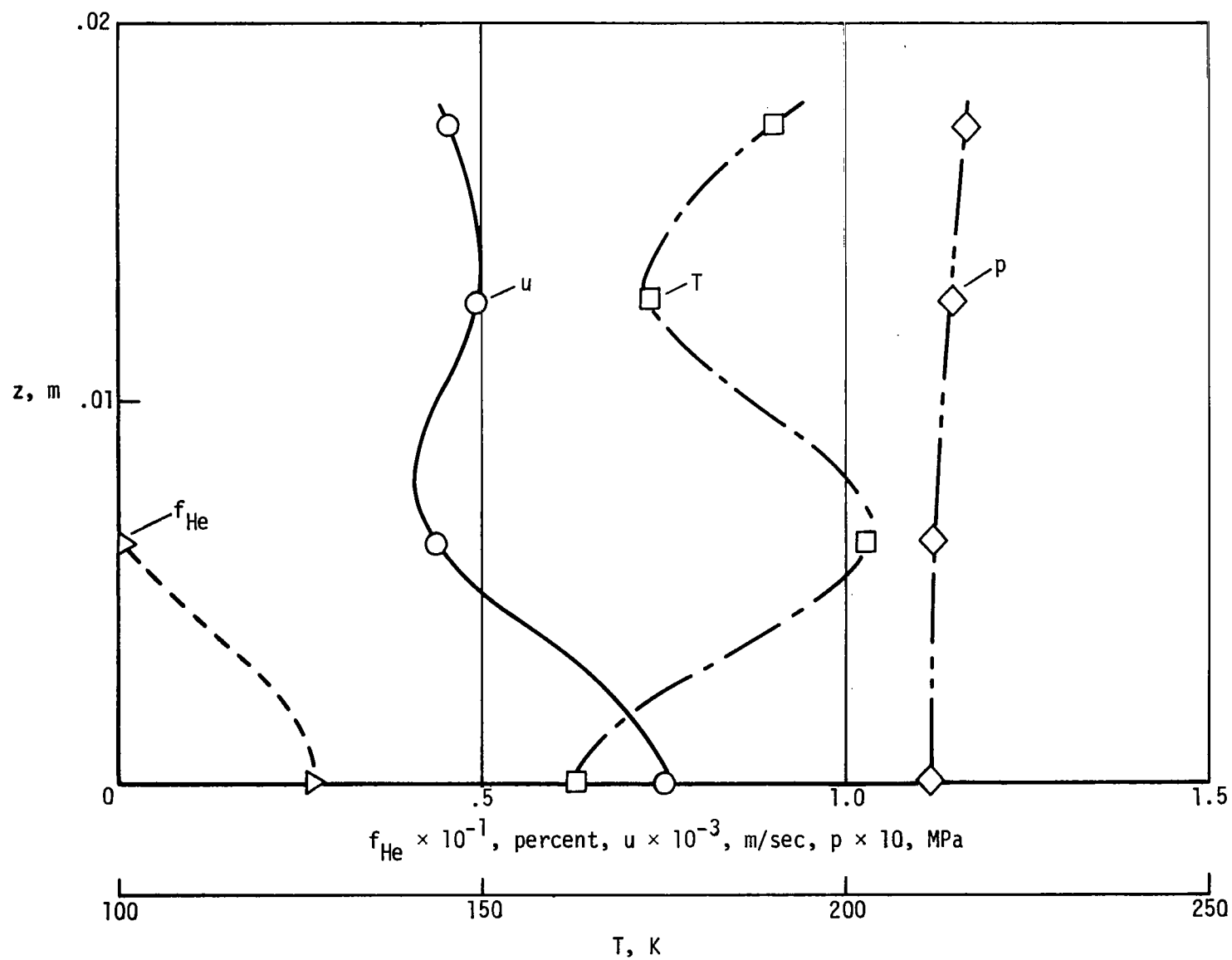


Figure 12.- Sketch of computational domains and coordinates.
All dimensions are in meters.



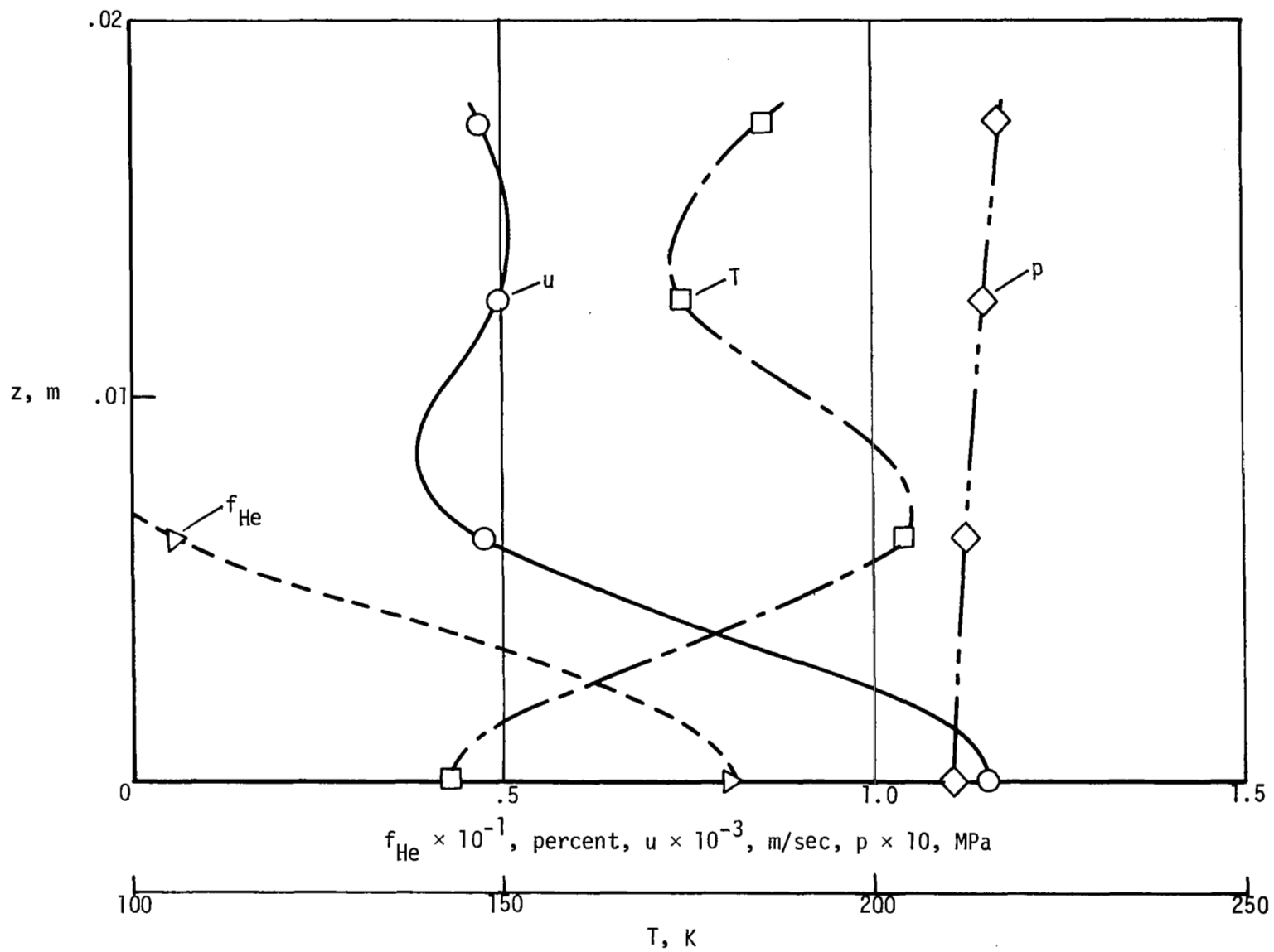
(a) $y = -0.0076$ m.

Figure 13.- Experimental flow variables at initial station ($x = 0.0421$ m).
Solid lines indicate interpolation.



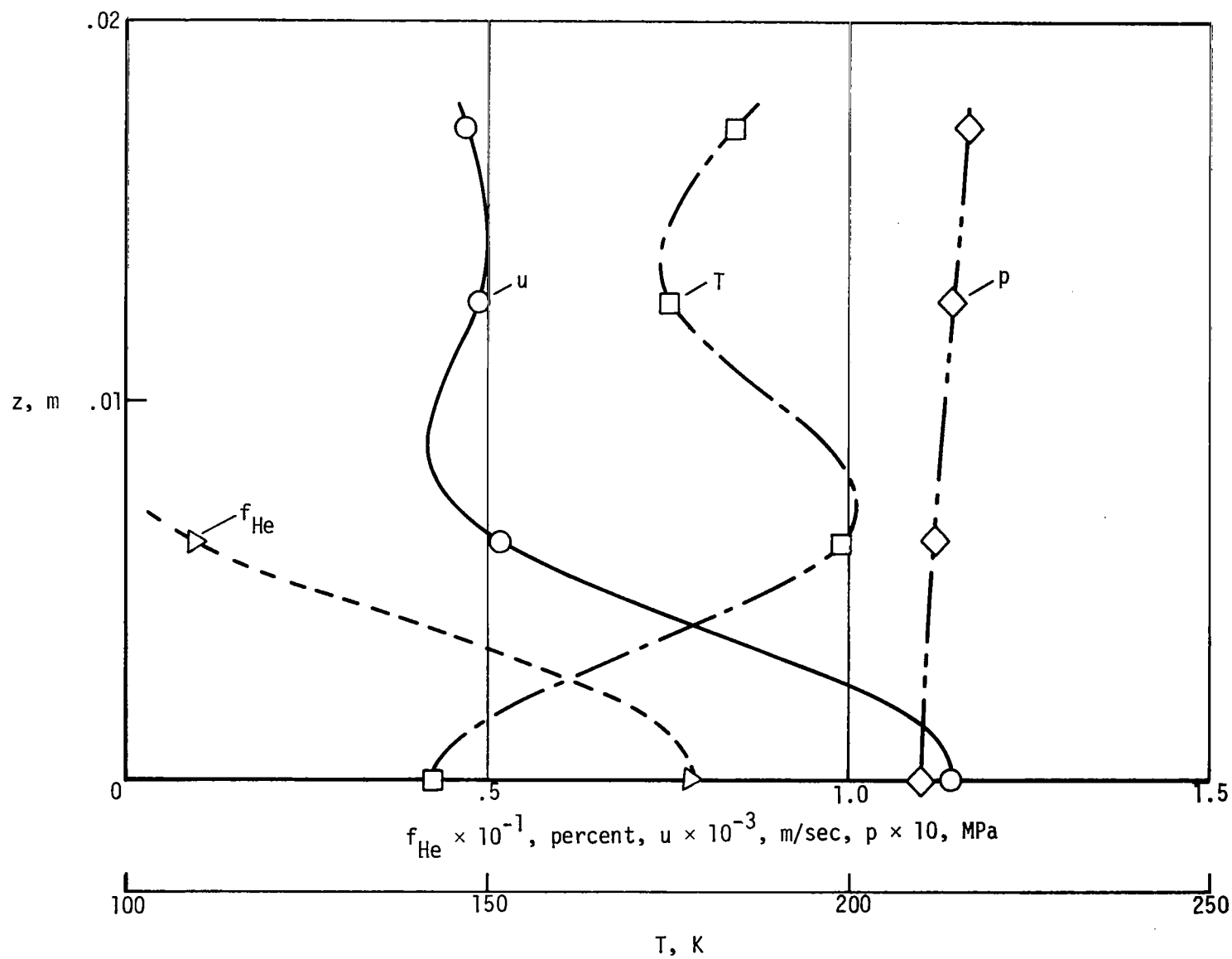
(b) $y = -0.0051$ m.

Figure 13.- Continued.



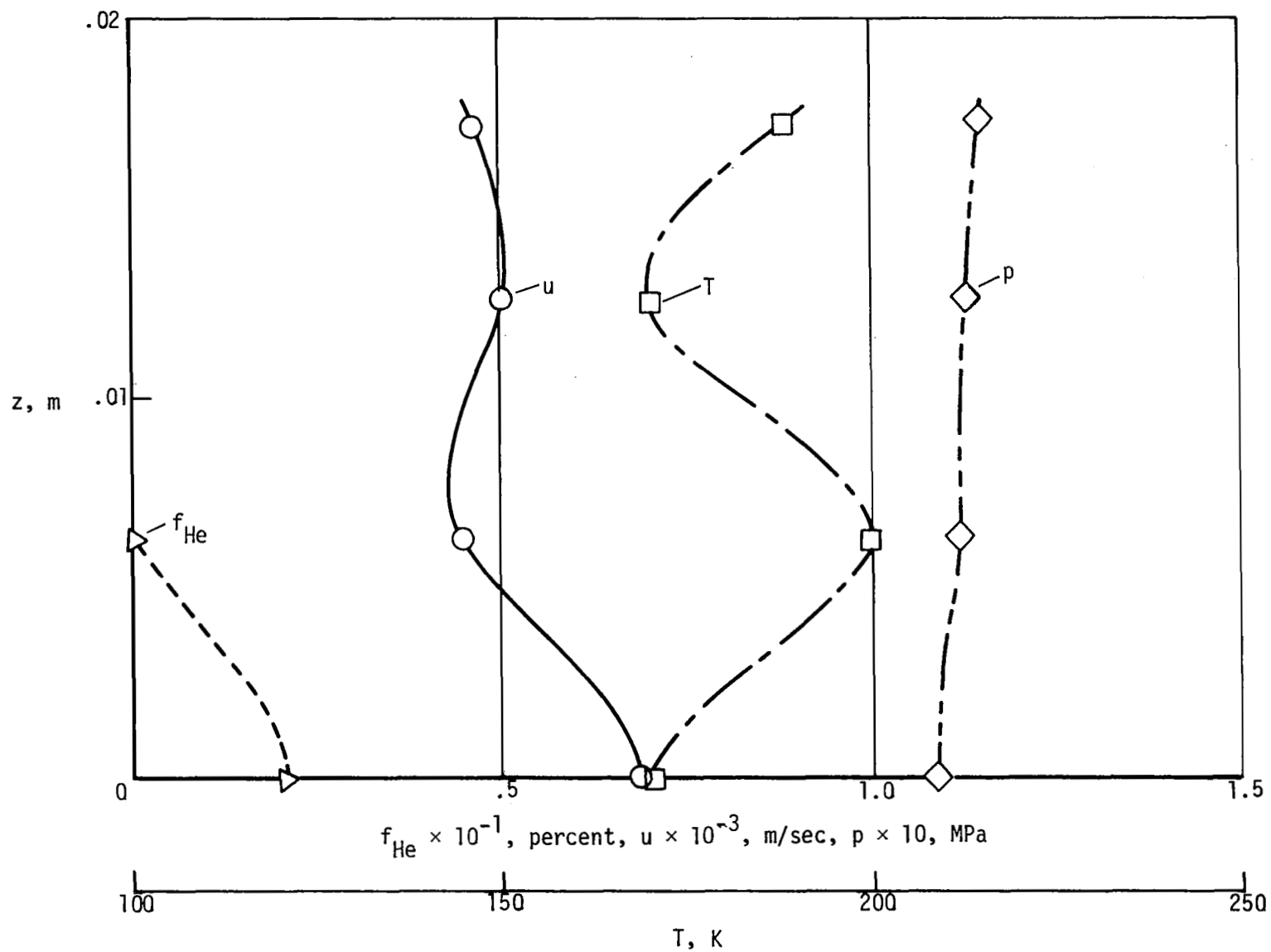
(c) $y = -0.0025$ m.

Figure 13.- Continued.



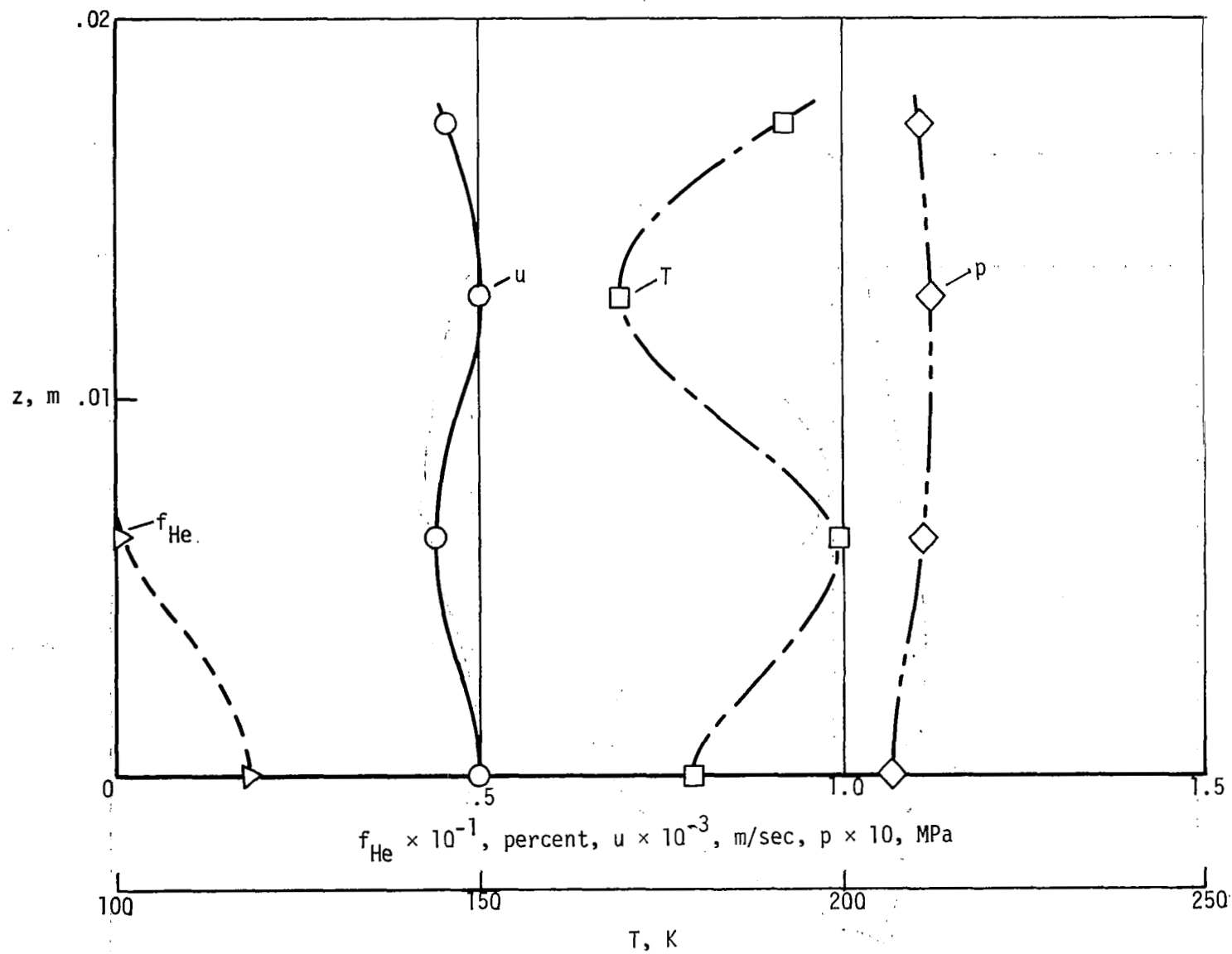
(d) $y = 0$.

Figure 13.- Continued.



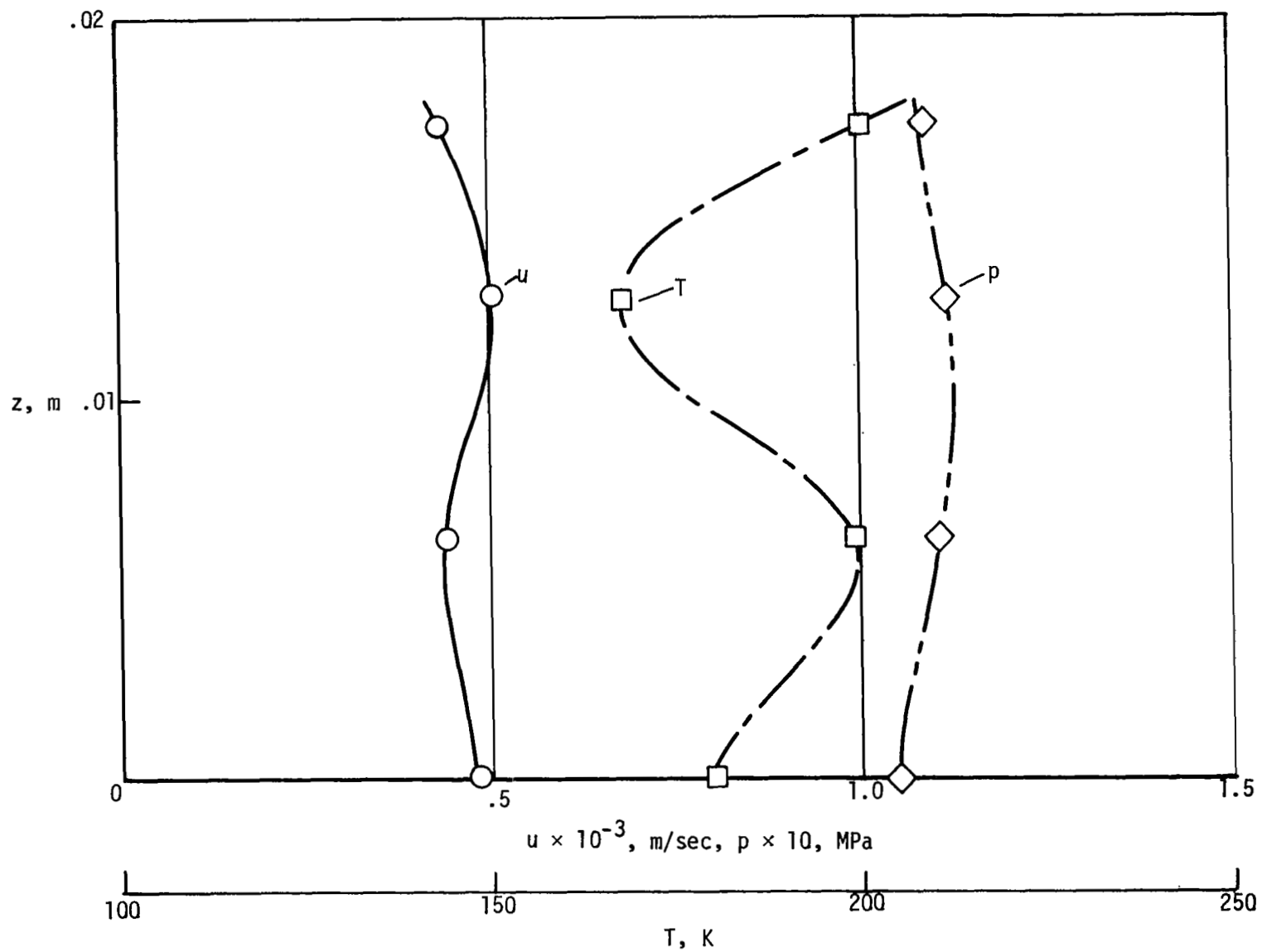
(e) $y = 0.0025$ m.

Figure 13.- Continued.



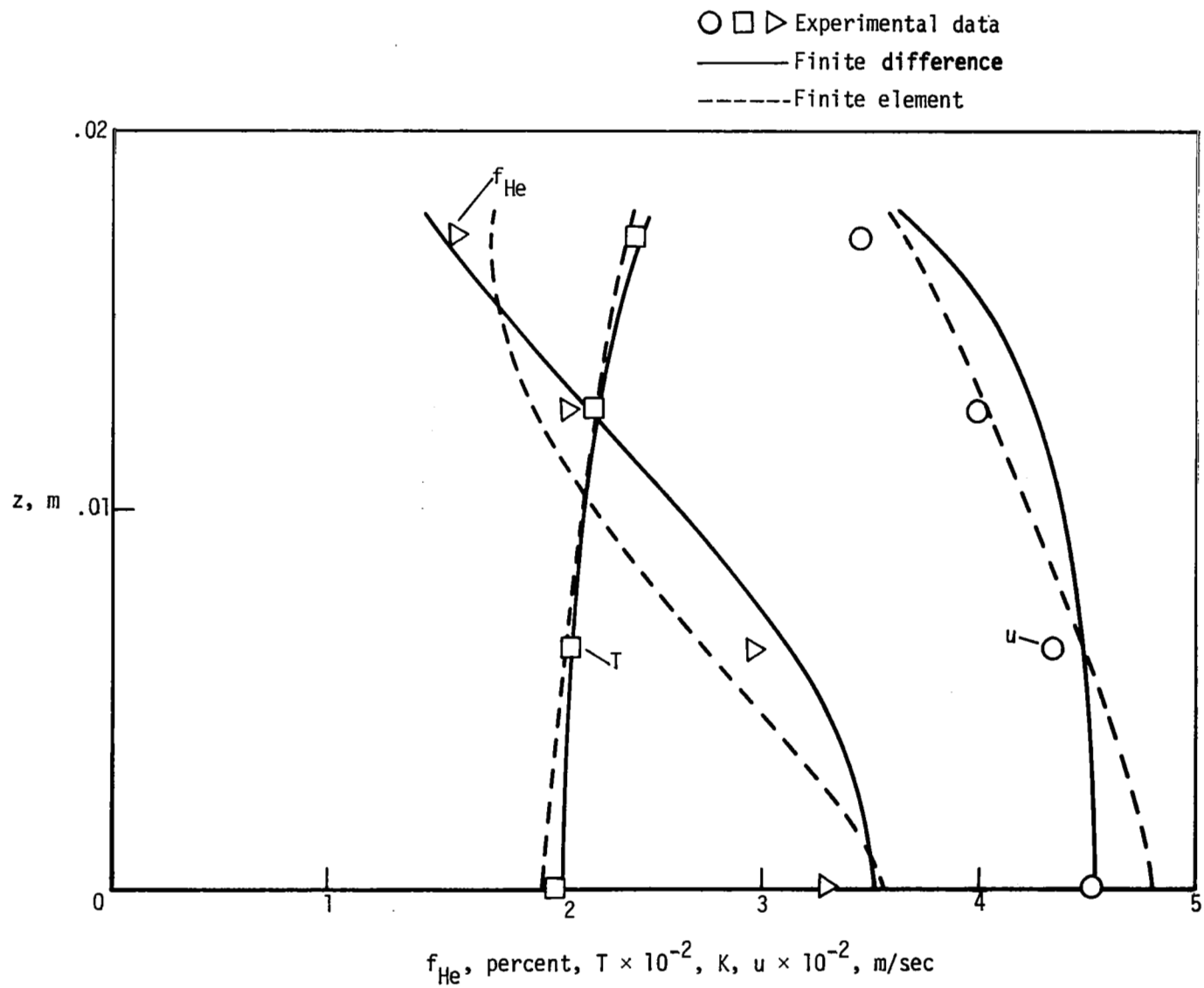
(f) $y = 0.0051$ m.

Figure 13.- Continued.



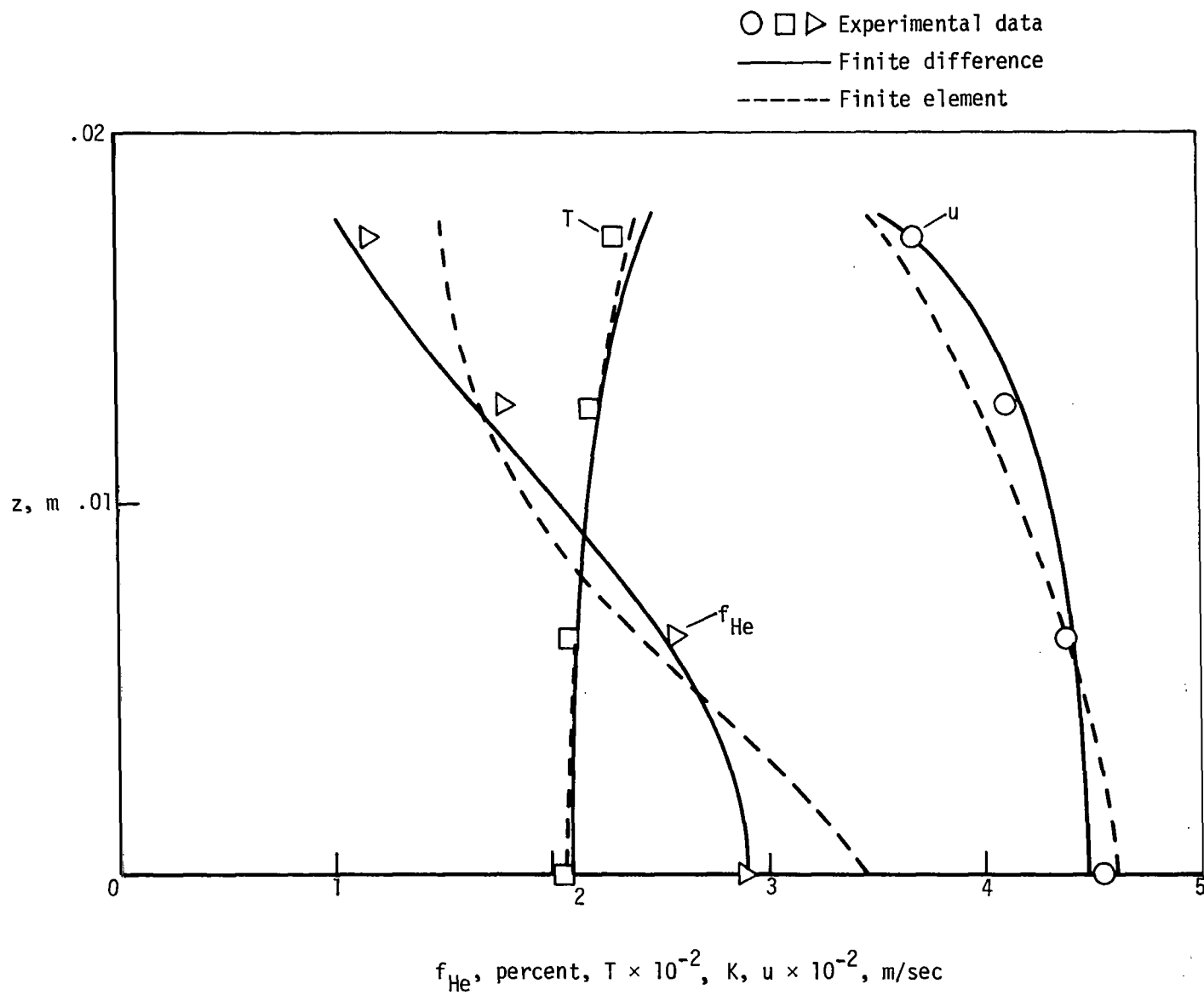
(g) $y = 0.0076$ m.

Figure 13.- Concluded.



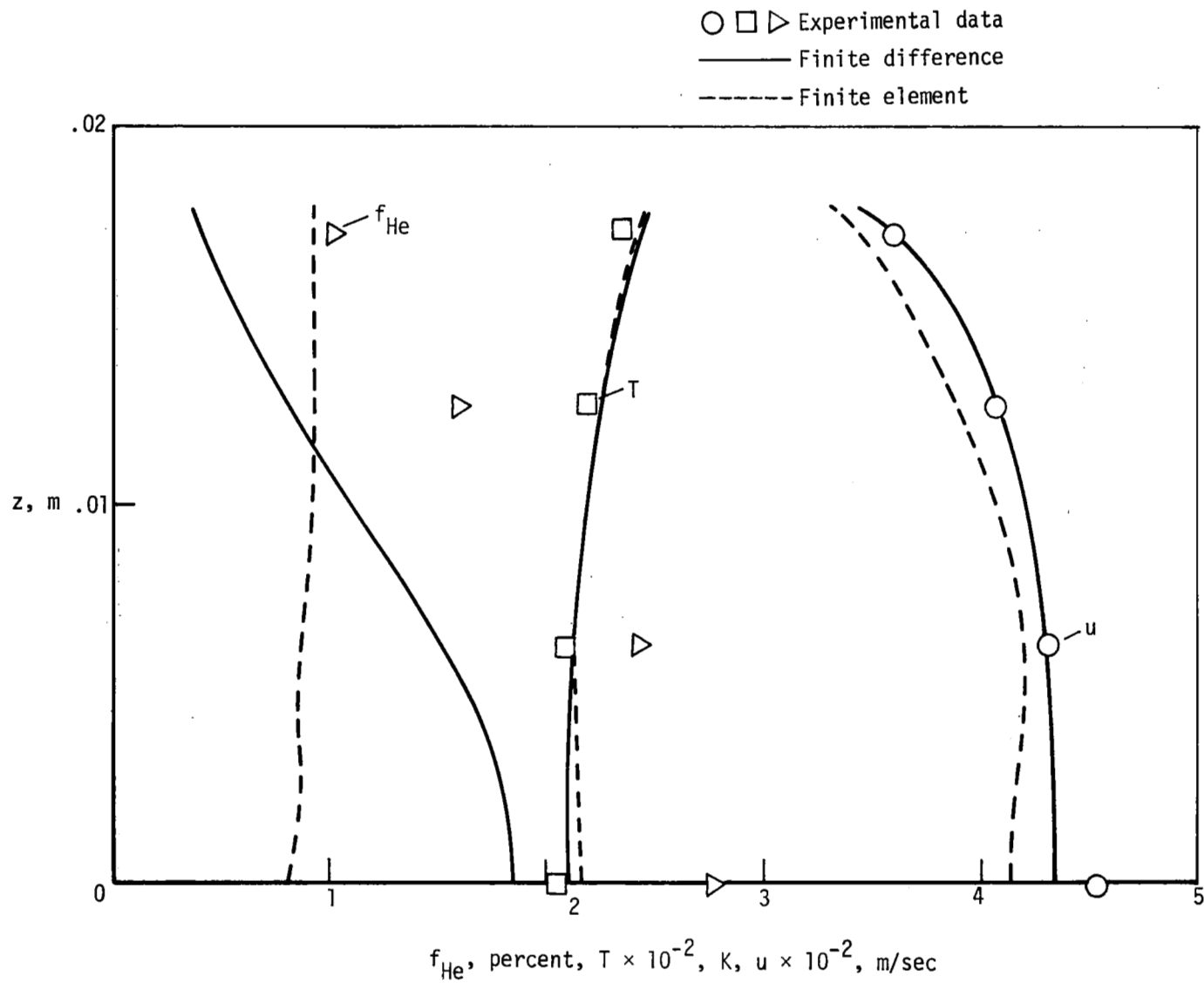
(a) $y = 0$.

Figure 14.- Comparison of computation and experimental results at downstream station ($x = 0.7369$ m).



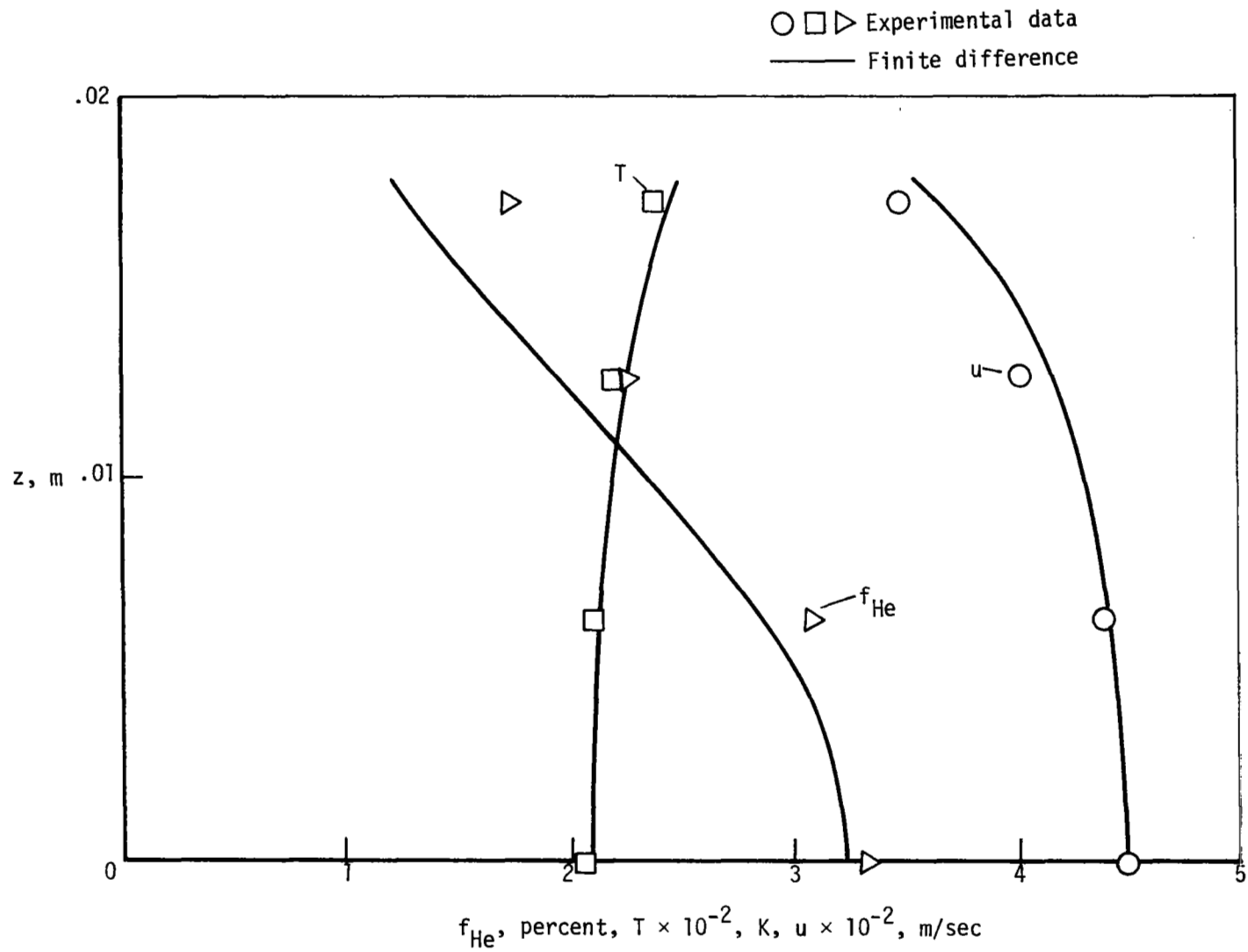
(b) $y = 0.0063$ m.

Figure 14.- Continued.



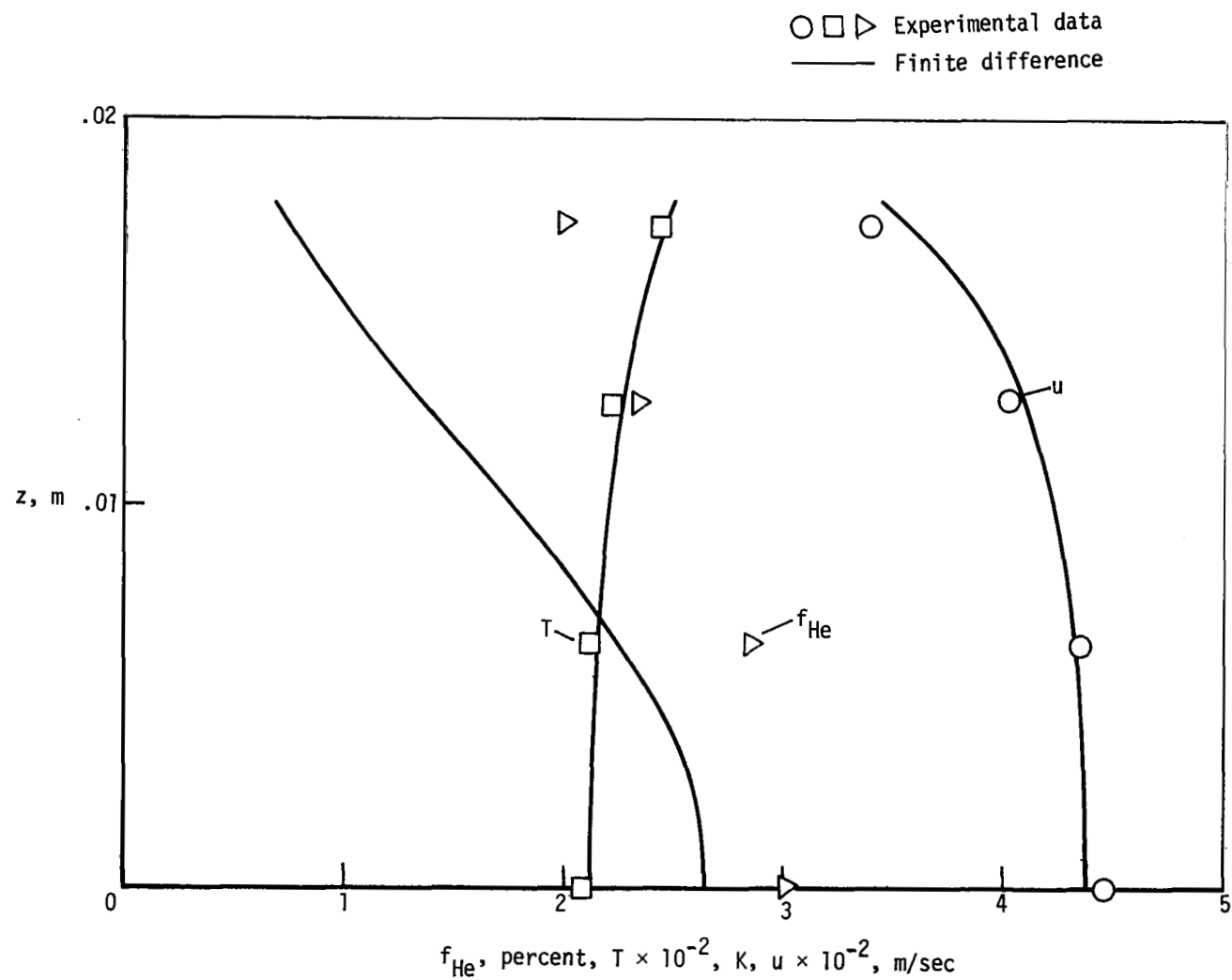
(c) $y = 0.0127$ m.

Figure 14.- Continued.



(d) $y = -0.0063 \text{ m}$.

Figure 14.- Continued.



(e) $y = -0.0127$ m.

Figure 14.- Concluded.

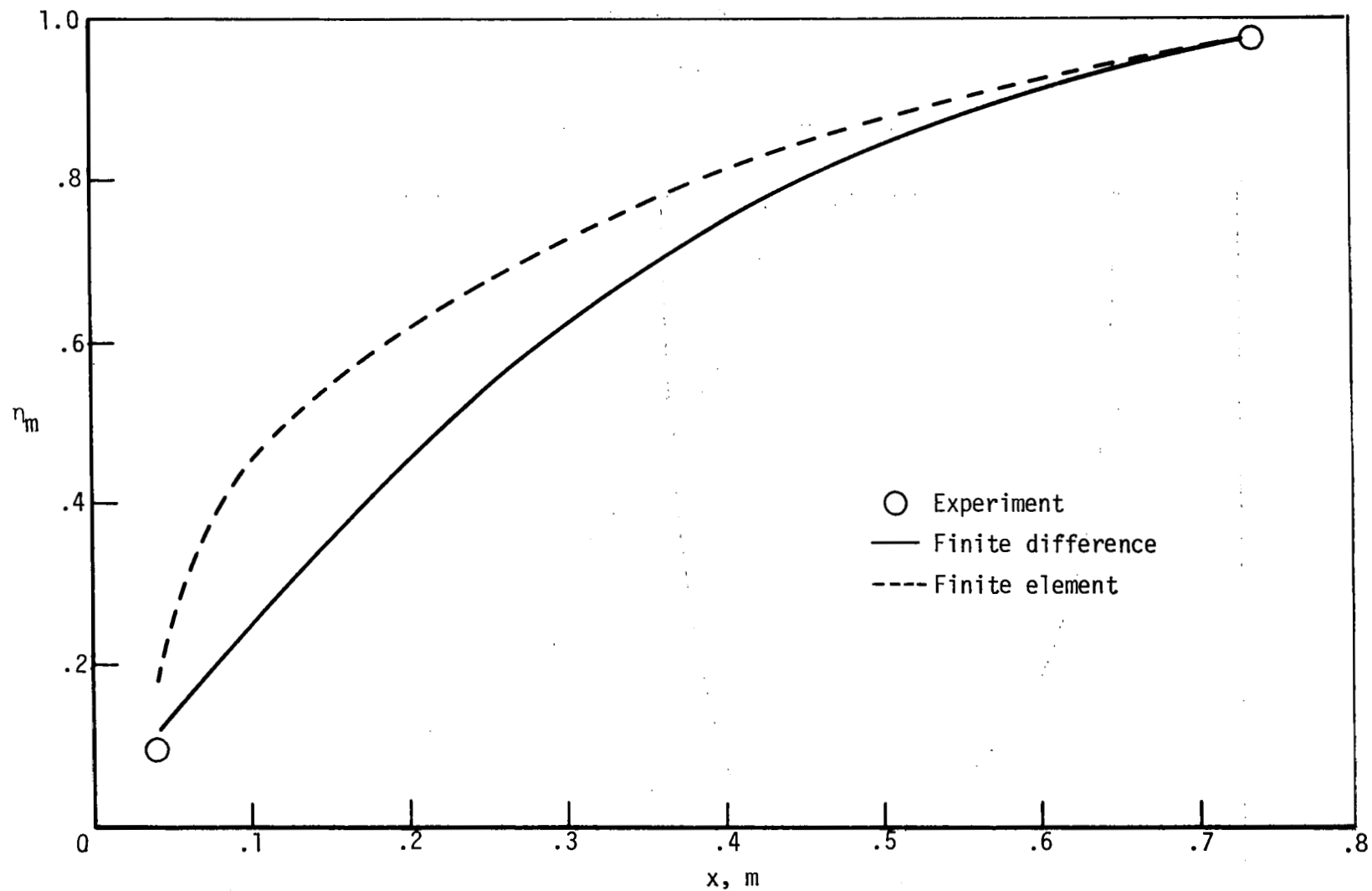


Figure 15.- Comparison of computational and experimental mixing efficiencies along combustion duct.

1. Report No. NASA TP-1166		2. Government Accession No.		3. Recipient's Catalog No.	
4. Title and Subtitle COMPARISON OF TWO COMPUTER PROGRAMS BY PREDICTING TURBULENT MIXING OF HELIUM IN A DUCTED SUPERSONIC AIRSTREAM				5. Report Date May 1978	
				6. Performing Organization Code	
7. Author(s) Y. S. Pan, John Philip Drummond, and Charles R. McClinton				8. Performing Organization Report No. L-11949	
				10. Work Unit No. 505-05-43-01	
9. Performing Organization Name and Address NASA Langley Research Center Hampton, VA 23665				11. Contract or Grant No.	
				13. Type of Report and Period Covered Technical Paper	
12. Sponsoring Agency Name and Address National Aeronautics and Space Administration Washington, DC 20546				14. Sponsoring Agency Code	
15. Supplementary Notes Y. S. Pan: NRC-NASA Senior Research Associate now with Department of Energy, Pittsburgh Energy Research Center, Pittsburgh, Pennsylvania. John Philip Drummond and Charles R. McClinton: Langley Research Center.					
16. Abstract Two parabolic flow computer programs, SHIP (a finite-difference program) and COMOC (a finite-element program), are used at the NASA Langley Research Center for predicting three-dimensional turbulent reacting flow fields in supersonic combustors. In this paper, the theoretical foundations of the two computer programs are described, and then the programs are applied to a three-dimensional turbulent mixing experiment. The cold (nonreacting) flow experiment was performed to study the mixing of helium jets with a supersonic airstream in a rectangular duct. Surveys of the flow field at an upstream station were used as the initial data by programs; surveys at a downstream station provided comparisons to assess program accuracy. Both computer programs predicted the experimental results and data trends reasonably well. However, the comparison between the computations from the two programs indicated that SHIP was more accurate in computation and more efficient in both computer storage and computing time than COMOC.					
17. Key Words (Suggested by Author(s)) Three-dimensional flow experiment Supersonic turbulent mixing Finite-difference computation Finite-element computation Fluid mechanics Numerical analysis			18. Distribution Statement Unclassified - Unlimited Subject Category 34		
19. Security Classif. (of this report) Unclassified	20. Security Classif. (of this page) Unclassified	21. No. of Pages 66	22. Price* \$5.25		

National Aeronautics and
Space Administration

Washington, D.C.
20546

Official Business

Penalty for Private Use, \$300

THIRD-CLASS BULK RATE

Postage and Fees Paid
National Aeronautics and
Space Administration
NASA-451



8 1 1U,D, 042078 S00903DS
DEPT OF THE AIR FORCE
AF WEAPONS LABORATORY
ATTN: TECHNICAL LIBRARY (SUL)
KIRTLAND AFB NM 87117

NASA

S

Verifiable (Section 158
Manual) Do Not Return